Scaling Laws of Fracture Network Properties in Crystalline Rock: a Powerful Approach to the Characterization of Unconventional Geofluids Reservoirs

A. Ceccato, G. Tartaglia, M. Antonellini, G. Viola

Corresponding author: Alberto Ceccato, alberto.ceccato@unibo.it

Dipartimento di Scienze Biologiche, Geologiche ed Ambientali – BiGeA, Alma Mater Studiorum – Università di Bologna – via Zamboni, 67, 40126 Bologna, Italy

Key points

- Multiscale analysis of hierarchical fracture network reveals different scaling properties for individual fracture sets and entire network
- Power-law scaling laws represent a predictive tool for the quantification of sub-seismic-resolution scale fracture distribution
- Multiscale, orientation-dependent analyses may improve the accuracy of permeability models of fractured reservoirs

Abstract

The multiscale analysis of fracture patterns helps to define the geometric scaling laws and the genetic relationships correlating outcrop- and regional-scale structures in a fracture network. Here we present the results of the multiscale analysis of the geometrical and spatial organization properties of the fracture network affecting the Rolvsnes granodiorite of the crystalline basement of southwestern Norway (Bømlo island). The fracture network shows a spatial distribution described by a fractal dimension $D \approx 1.51$, with fracture lengths distributed following a power-law scaling law (exponent $\alpha = -1.95$). However, orientation-dependent analyses show that the identified fracture sets vary their relative abundance and spatial organization with scale, defining a hierarchical network. Fracture length, density, and intensity of each set vary following power-law scaling laws characterized by their own exponents. Comparing the results from each set with those generated from the entire network, we discuss how the obtained scaling laws improve the accuracy of resolving sub-seismic-resolution scale structures, which steer the local-scale permeability of fractured reservoirs. As documented in the field, the identified fracture sets affect the fractured basement permeability differently. Thus, results of multiscale, orientation-dependent statistical analyses, integrated with field analyses of fracture lineaments, can effectively improve the detail and accuracy of permeability prediction of fractured reservoirs. Our results show also how regional geology and analytical biases affect the results of multiscale analyses and how they must be critically assessed before extrapolating the conclusions to any other similar case study of fractured unconventional geofluids reservoirs.

Keywords

Fracture network, Multiscale analysis, Power-law distributions, Fracture length distribution, Sub-seismic-resolution scale.

Plain Language Summary

Fracture and fault zones represent the preferential pathways for fluid flow in igneous and metamorphic rocks, which are commonly characterized by very low intrinsic permeability. In particular, the fractures observed at the outcrop seem to enhance the permeability of such rocks much more than larger-scale fracture and fault zones do. Where fracture networks are well exposed on the Earth surface, they can be mapped at different scales and their spatial distribution and geometrical characteristics quantified. This allows us to retrieve mathematical relationships describing the variation of spatial and geometrical properties across different scales of observation, which can be then adopted to quantify the spatial and geometrical characters of fracture networks at any scale and, in particular, the intensity and geometry of fractures at the outcrop scale. In addition, field analyses taught us that each set of the identified fracture and fault zones affects the permeability of the fractured rock at the outcrop scale in a different manner. The adoption of these mathematical laws, therefore, can aid to quantitatively constrain the variation of permeability of the fractured rock as well.

1. Introduction

Fractured crystalline basement units are attracting increasing interest as potential unconventional reservoirs for natural georesources (oil, heat, and water) and as potential disposal or storage sites (nuclear waste, CO_2, H). Crystalline rocks are characterized by very low intrinsic permeability, usually in the order of 10^{-18} m^2 (Achtziger-Zupančič et al., 2017; Brace, 1984), such that their capability to transmit and/or store fluids is mainly related to the structural permeability associated with fracture and fault networks developed during brittle deformation (Ceccato, Viola, Antonellini, et al., 2021; Ceccato, Viola, Tartaglia, et al., 2021; Pennacchioni et al., 2016; Schneeberger et al., 2018; Stober & Bucher, 2015). Fracture and fault networks exhibit variable geometrical and spatial characteristics, which need to be assessed and, if possible, quantified to evaluate their effective control on the permeability of the rock mass. Indeed, fractures at different scales may affect and steer fluid flow and reservoir compartmentalization very differently (Le Garzic et al., 2011; Hardebol et al., 2015). For example, long-lived composite fault zones defining regional-scale structures usually control the large-scale compartmentalization of reservoirs (Holdsworth et al., 2019). Being usually identified by means of standard seismic investigations, these structures are generally referred to as Seismic-Resolution Scale (SRS) structures (Tanner et al., 2019). On the other hand, small scale fracture networks, including limited-throw fractures and faults, control the permeability at the outcrop- or borehole-scale (Damsleth et al., 1998; Walsh et al., 1998). These structures are usually not detected and thus imaged by standard seismic investigations, and are therefore referred to as Sub-Seismic-Resolution Scale (SSRS) structures (Tanner et al., 2019). SRS and SSRS structures occurring in a specific region or rock volume are, likely, genetically related and share common characteristics in term of their geometry, spatial organization, and hierarchical relationships (e.g., Holdsworth et al., 2020; McCaffrey et al., 2020).

Usually, a multiscale analysis of a fractured medium is adopted to quantify the geometrical characteristics of its fracture network at different scales. Additionally, this approach is necessary to

derive mathematical functions, i.e., scaling laws, that describe and constrain the distribution (in terms of density, intensity, relative proportions) of the geometrical features (e.g., length, spacing, throw) of the fracture network across scales (Bossennec et al., 2021; Chabani et al., 2021; Dichiarante et al., 2020; McCaffrey et al., 2020). Scaling laws described by a power-law function can effectively account for the distribution properties of the network at a variety of scales, assuming seamless self-similarity and scale-invariancy of the studied geometrical properties (Bonnet et al., 2001). Nonetheless, self-similarity may actually be limited to only specific scale ranges that are defined by an upper and lower dimensional bound and a characteristic length scale. Also, significant deviations from self-similarity are typical of fracture networks in mechanically layered geological systems, wherein anisotropic mechanical properties, fracture mechanics, and characteristic length scales of the layers may control the development of preferential fracture geometries or spatial organizations (Castaing et al., 1996; Kruhl, 2013; Laubach et al., 2009; Soliva et al., 2006). In those cases, the upscaling of geometrical properties is better performed by adopting other scaling laws such as, for example, negative exponential, log-normal or gamma-law that specifically refer to the identified scale range of pertinence (Bonnet et al., 2001). Conversely, previous authors have suggested that the power-law distribution of both fracture length and spacing is typical of fracture networks within massive crystalline rocks lacking pervasive heterogeneities (Gillespie et al., 1993; McCaffrey et al., 2020; Odling et al., 1999).

Here we report the results of the multiscale analysis of lineament maps representing the fracture network deforming the crystalline basement of the island of Bømlo (Western Norway). Fracture network maps were obtained from the manual picking of lineaments on LiDAR digital terrain models, aerial and UAV-drone orthophotos of the exposure area of the Rolvsnes granodiorite (Fig. 1). The fractured (and weathered) crystalline basement exposed in Bømlo is thought to represent the on-shore analogue of an offshore unconventional oil reservoir hosted in the Utsira High in the North Sea (Fredin et al., 2017; Riber et al., 2015; Trice et al., 2019). The fracture network within the

Rolvsnes granodiorite represents a good example of fracture network developed during a prolonged brittle tectonic history within massive, isotropic granitoid rocks. The in-situ analysis and characterization of representative constituents of this fracture and fault zones network, e.g., the Goddo Fault Zone (GFZ, Fig. 1), has previously allowed us to reconstruct in detail the timing of deformation and to quantify its fracture geometry and petrophysical properties (Ceccato, Viola, Antonellini, et al., 2021; Ceccato, Viola, Tartaglia, et al., 2021; Scheiber & Viola, 2018; Viola et al., 2016). This notwithstanding, the larger-scale geometry and organization of these fracture and fault network remain poorly constrained and need quantification.

Our statistical analysis of the fracture network properties was conducted at different scales of observation aiming to identify the scaling relationships (if any) for each analyzed property. Fracture network properties include: (i) fractal dimension D; (ii) lineament orientation; (iii) cumulative length distribution of lineaments at each scale and for each orientation set; (iv) intensity/density scaling for the whole lineament network and for each orientation set. The ultimate goal is to characterize in detail the scaling relationships (and understand their limitations) for the geometrical properties of the Rolvsnes fracture network as a possible analogue for the fracture network documented in the offshore Utsira High unconventional oil reservoir hosted in a fractured and weathered crystalline basement (Fredin et al., 2017; Trice et al., 2019). These analyses represent a powerful tool for the identification of SSRS structures, the quantification of their heterogeneous distribution and, accordingly, the heterogeneous distribution of permeability of the fractured crystalline basement at different scales. The implications of the adoption of general scaling laws on the upscaling/downscaling of fracture network properties, as well as the possible analytical biases and sources of errors in the analytical approach, are finally evaluated and discussed.

2. Geological setting

The crystalline basement of Bømlo belongs to the Upper Allochthon units of the Caledonian orogen (Gee et al., 2008). Our lineament maps represent the fracture pattern affecting the Rolvsnes

129 granodiorite, a pre-Scandian (466 ± 3 Ma; zircon U-Pb dating) granitoid pluton hosted in the Upper
130 Allochthon metamorphic units (Scheiber et al., 2016) (Fig. 1). The Rolvsnes granodiorite recorded a
131 prolonged and multi-phase brittle deformation history (Scheiber et al., 2016; Scheiber & Viola,
132 2018), only briefly summarized in the following, while the reader is referred to the cited literature
133 for a more detailed and comprehensive description of the tectonic history of the area. Overall, the
134 whole tectonic history of the area is the expression of three main deformation episodes (Bell et al.,
135 2014; Fossen et al., 2016, 2021): (1) Caledonian convergence and continental collision from the
136 Mid-Ordovician to the Silurian; (2) extensional tectonics related to the late-Scandian orogenic
137 collapse during the Devonian, and (3) prolonged and multi-phase extensional tectonics related to the
138 North Sea rifting from the Permian to the Cretaceous. During this tectonic evolution, the pre-
139 Scandian Rolvsnes granodiorite did not record penetrative ductile strain and was instead affected by
140 pervasive brittle deformation. Each tectonic stage has been related to a characteristic set of fracture
141 and fault zones that dissect Bømlo (Scheiber & Viola, 2018): (1) NNW- and WNW-striking
142 conjugate strike-slip faults developed coevally with ENE-WSW-striking reverse faults during
143 Caledonian convergence; (2) the same structures were reactivated with opposite kinematics during
144 the early stages of late-Scandian orogenic collapse; (3) NW- and NNW-striking normal faults
145 ascribable to the regional Permian-to-Jurassic rifting phase of the North Sea, which partially
146 reactivated earlier, inherited structures. During the latest rifting stages of the North Sea, in the Early
147 Cretaceous, new and N- to NNE-striking fracture corridors and normal faults overprinted the
148 previously formed fracture pattern. Indeed, our lineament maps depict efficiently the complex and
149 multiscale network of fractures and fault zones affecting the crystalline basement of Bømlo, which
150 have been repeatedly reactivated during the prolonged rifting history of the North Sea (Ceccato,
151 Viola, Tartaglia, et al., 2021; Scheiber & Viola, 2018; Viola et al., 2016).

152 A key structure for the detailed analysis of the timing of deformation, the geometry of the
153 deformation structures, and the effects of deformation on the petrophysical properties of the

154 crystalline basement of Bømlo, is the Goddo Fault Zone (Fig. 1), (Ceccato, Viola, Antonellini, et
155 al., 2021; Ceccato, Viola, Tartaglia, et al., 2021; Scheiber & Viola, 2018; Viola et al., 2016). The
156 Goddo Fault Zone is an east-dipping normal fault that accommodated multiple slip increments
157 during the prolonged Permian-to-Cretaceous rifting of the North Sea, recording several stages of
158 reactivation, during which a complex network of brittle structural facies developed in the fault core
159 (*sensu* Tartaglia et al., 2020). Structures like the Goddo Fault Zone actually controlled the
160 permeability and fluid flow evolution from rifting to current times of the crystalline basement
161 (Ceccato, Viola, Antonellini, et al., 2021; Ceccato, Viola, Tartaglia, et al., 2021; Viola et al., 2016).

162 Similarly to Bømlo, a complex fracture and fault network developed in the crystalline basement of
163 the Utsira High, of which the Rolvsnes granodiorite is interpreted as the onshore analogue (Fredin
164 et al., 2017; Trice et al., 2019). The Utsira High crystalline basement is composed of (likely
165 multiple) pre-Scandian igneous intrusions of similar age and composition to the Rolvsnes
166 granodiorite (Lundmark et al., 2014; Slagstad et al., 2011). The fracture network in the Utsira High
167 developed under tectonic conditions similar to those of the Bømlo crystalline basement, but with
168 several significant differences mainly related to the structural position of the two crystalline
169 basements within the North Sea rifting region (Bell et al., 2014).

170

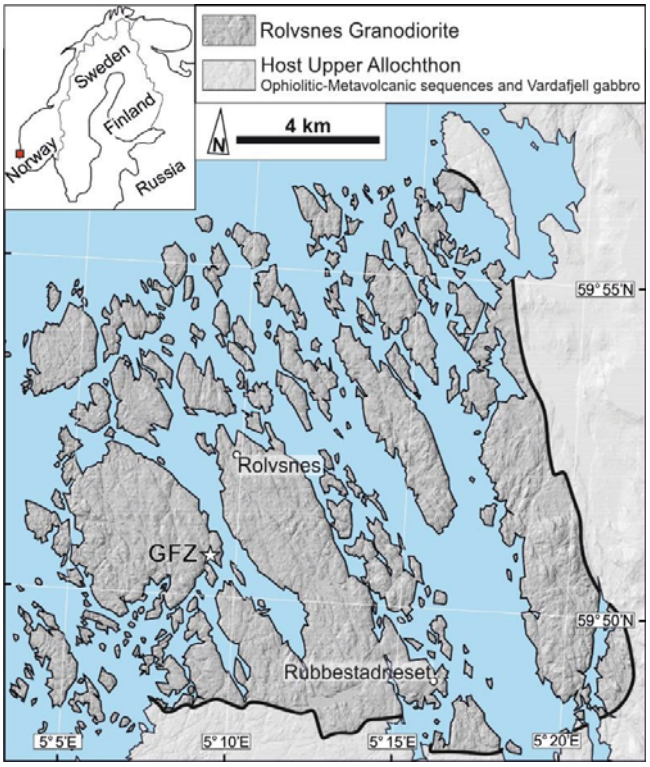

Figure 1.

Simplified geological map of the Bømlo Island reporting the area where the Rolvsnes granodiorite crops out overlaying the Digital Terrain Model obtained from high-resolution (1 m) LiDAR survey.

3. Materials and Methods

The fracture/lineament maps (Fig. 2a) used for the multiscale analyses presented here have been generated in ArcGIS 10.8 by manually picking the same digital terrain model (DTM) of selected areas of Bømlo at different scales of observation. DTM's from high-resolution (1 m) airborne Light Detection and Ranging (LiDAR) surveys (Fig. 1) have been used for the manual picking of fracture lineaments at the 1:5,000; 1:25,000 and 1:100,000 scales. The details of LiDAR data acquisition and DTMs elaboration can be found in Scheiber et al. (2015). In addition, the dataset of fracture lineaments interpreted from LiDAR DTM at the 1:5,000 scale was integrated with the interpretation of aerial orthophotos from the Bing Maps database (https://www.bing.com/maps). Bing aerial imagery was also adopted to distinguish between natural and man-made linear structures and to check for artefacts and potential misinterpretation of linear features on LiDAR-derived DTMs in the absence of systematic ground truthing. The outcrop-scale lineament picking was performed on digital orthophotos of a key Goddo Fault Zone outcrop (Figs. 1, 3a) as obtained from the elaboration of the imagery collected via UAV-drone surveys through Structure-from-Motion (SfM) algorithm. Details on this acquisition and its elaboration methods can be found in Ceccato, Viola, Antonellini, et al. (2021). Topographic lineaments were traced as single, linear segments (not polylines) interpreting their topographic expression on DTMs. This interpretation technique introduces two major analytical biases on the obtained lineament maps: 1) the interpreted length may only partially represent the entire lineament (which may be covered by deposits or be differently expressed in the topography, thus being not visible in its entire length, e.g., Cao & Lei, 2018); 2) as a consequence, abutting relationships, intersections between lineaments and lineament network topology and connectivity remain highly speculative and susceptible to subjective biases (Andrews et al., 2019). The orientation of mapped lineaments, expressed as azimuth angle from the geographic north, was calculated in ArcGIS 10.8 using the freely available tool Easy Calculate 10 (https://www.ian-ko.com/free/free_arcgis.htm) and the Orientation Analysis Tools (https://is.muni.cz/www/lenka.koc/prvnistrana.html). Rose diagrams plotting lineament azimuths

were produced with the MARD 1.0 software (Munro & Blenkinsop, 2012). Lineament density P_{20} (m^{-2}) and intensity P_{21} (m/m^2) (Dershowitz & Herda, 1992) were calculated as the ratio between the total number of lineaments and total length of lineaments, respectively, over the total area of the land exposure in each lineament map.

3.1. Fractal dimension – Box-counting method

The fractal dimension of each lineament map at different scales was computed with the box-counting method (Bonnet et al., 2001; Gillespie et al., 1993), adopting the freely available function boxcount.m in MATLAB R2019b (http://www.fast.u-psud.fr/~moisy/ml/boxcount/html/demo.html). The box-counting method consists in subdividing the analyzed image in progressively smaller square boxes of side *b* and counting how many of them contain a segment of the analyzed lineament network. Plotting the number *n* of boxes containing at least one lineament against the side length *b* on a log-log diagram should yield a straight curve, whose slope defines a power-law function with *D* as the fractal exponent (Bonnet et al., 2001). The fractal dimension obtained from the box-counting method quantifies the scaling properties of the spatial occupancy of the fracture network (Bonnet et al., 2001).

3.2. Cumulative length distribution analyses

Length data of lineaments extracted from lineament maps have been organized as cumulative distributions and plotted in log-log diagrams of the length L of lineaments on the X-axis versus the cumulative number N of lineaments with length $l > L$ (Fig. 2b-c). The cumulative length distributions were then normalized by the area of the land surface reported on each map over which the lineaments were picked. Cumulative length distributions have then been analyzed by means of the Maximum Likelihood Estimation (MLE) and Kolmogorov-Smirnov (KS) statistical tests to retrieve the best fitting mathematical function (Dichiarante et al., 2020; Kolyukhin & Torabi, 2013; Rizzo et al., 2017). The mathematical functions considered were negative exponential, power-law and log-normal (Fig. 2b). The advantage of adopting MLE-KS statistical tests derives from the

possibility to also retrieve the function parameters (namely the exponent λ for the exponential, the exponent α for the power-law and the mean μ and standard deviation σ for the log-normal functions) in addition to the mathematical function best approximating the observed cumulative length distributions. A dedicated MATLAB script implementing the freely available functions provided in the latest version of FracPaQ (Healy et al., 2017; Rizzo et al., 2017) was used to this purpose. The results of the MLE-KS analyses are presented as "checkerboard" diagrams, following the method proposed by Dichiarante et al. (2020) (Fig. 2d). Such diagrams allow to image the results of the MLE-KS analyses performed on the selected portions of the cumulative distribution, i.e., the best fitting mathematical function for variable subdomains of the cumulative distribution. A subdomain is defined as a segment of the cumulative distribution curve bounded by a lower and upper cut value (Fig. 2c-d). The upper cut value represents the distance, expressed in terms of percentage of the total number of elements contained in the cumulative distribution, from the shortest observed length. The lower cut value represents the distance, in terms of percentage of the total number of elements contained in the cumulative distribution, from the longest observed length. On the checkerboard diagrams, the lower cut values are plotted versus the upper cut values (Fig. 2d). Each point of the checkboard therefore represents a specific percentage range of the total cumulative distribution between the upper and lower cut limits over which the MLE-KS tests have been run. The plotted symbol represents the mathematical function among those considered (power-law, exponential, log-normal) for which the MLE-KS tests yielded the highest fitting score, whereas the symbol is color-coded according to the retrieved value of the fitting scores (namely HP and PP parameters, see Rizzo et al., 2017; Dichiarante et al., 2020). This analytical approach allows to determine the mathematical function that best fits the truncated cumulative distribution and to evaluate the effect of truncation and censoring biases (Fig. 2c-d). The MLE-KS analyses were performed for the cumulative length distribution of the entire set of lineaments contained in each map at each scale of observation (1:100; 1:5,000; 1:25,000; 1:100,000) and for the cumulative distributions of lineaments classified according to their orientation for each scale. In addition, the

cumulative length distributions representing the entire population of each lineament map and each lineament set at different scales of observation have been plotted on a cumulative log-log diagram in order to evaluate the "general" relationship that may link cumulative distributions observed at different scales.

3.3.Spatial distribution analysis

The spatial distribution of lineaments has been quantified by following the approach by Sanderson and Peacock (2019). We analyzed the statistics of spacing between lineaments collected along virtual scanlines computed with the NetworkGT toolkit in QGis 3.12.2 (Nyberg et al., 2018) (e.g., Fig. 2e). The lineaments were classified and grouped into orientation sets according to the results of the orientation analysis. A grid of equally-spaced virtual scanlines oriented perpendicular to the selected lineament set orientation was draw upon the imported lineament map with NetworkGT (e.g., Fig. 2e). With NetworkGT we collected and analyzed the intersections between each virtual scanline and the lineaments reported on the map. For each scanline, we analyzed the statistics (average value, standard deviation – 2σ, minimum and maximum values) of several parameters (Fig. 2e): (i) spacing (S) between two intersected lineaments; (ii) Coefficient of Variation (CoV) of the spacing, defined as the ratio between the standard deviation of spacing along a scanline and its average ($CoV = \sigma S/\langle S \rangle$) (Gillespie et al., 1993); (iii) coefficient of heterogeneity (V_f) and its statistical significance (V*) according to Sanderson and Peacock (2019). The Coefficient of Variation (CoV) of spacing is commonly adopted to assess the spatial organization (clustering vs. uniform distribution) of fractures along linear scanlines (e.g. Gillespie et al., 1993). In particular, CoV values > 1 are usually related to the occurrence of clustered fracture distributions; CoV = 1 should represent a (negative) exponential-random distribution of spacing intervals, and CoV < 1 is usually related to log-normal (uniform) spacing distributions (Gillespie et al., 1993; McCaffrey et al., 2020; Odling et al., 1999). The spacing heterogeneity, i.e., the deviation of the spacing distribution along a scanline from a uniform distribution, is quantified by the V_f and V*

coefficients, as computed by adopting the method by Kuiper (Sanderson & Peacock, 2019). The coefficient of heterogeneity V_f quantifies the deviation from a theoretical uniform distribution of the observed spacing distribution along a given scanline expressed as the sum of the moduli of the positive and negative deviations (see Sanderson and Peacock, 2019; Fig. 2e). The coefficient V* quantifies the statistical significance of the heterogeneity factor V_f:

$$V^* = V_f \left(\sqrt{N} + 0.155 + \frac{0.24}{\sqrt{N}}\right);$$

where N represents the number of intersected fractures along the scanline. As reported in Sanderson & Peacock (2019), "Stephen (1970) showed that if V* > 1.75, 2.0 and 2.3, one can reject the null hypothesis of uniformity at the 95%, 99% and 99.9% levels, respectively". Thus, the coefficient V* can be used to quantify the probability that a certain spacing distribution is uniform or not. We have performed a combined analysis of CoV and V* because of the limited amount of intersections recorded by each virtual scanline (<< 30 fractures per scanline) in our maps. For the same reason, more advanced and up-to-date analyses of the spacing variability (e.g., Marrett et al., 2018; Sanderson & Peacock, 2019; Bistacchi et al., 2020) were not possible. We present the results of this analysis in CoV-V* diagrams (e.g., Fig. 2f), wherein the coefficient of variation of spacing is plotted against the statistical significance of the spacing heterogeneity computed with the Kuiper's method. The statistical distribution of the CoV and V* values characterizes the general spatial organization of each orientation set of lineaments (Sanderson & Peacock, 2019). Plotting the statistical distribution (box-and-whiskers) of the values of CoV vs. V*, we can qualitatively evaluate if, statistically, a set of fractures tends to present a random or organized spatial distribution. With this method, four main spatial organization types can be distinguished (Fig. 2f): (i) Uniform distribution, characterized by CoV << 1 and V* < 1.75; (ii) random distribution, characterized by CoV ≈ 1, V* < 1.75; (iii) Corridor-Clustered distribution, characterized by CoV > 1 and V* > 1.75-2.00; (iv) Fractal distribution, characterized by CoV >> 1 and V* >> 1.75-2.00. Scanlines with

more than 10, 5 and 3 intersections were considered for the analysis of lineament maps at 1:5,000, 1:25,000, 1:100,000, respectively.

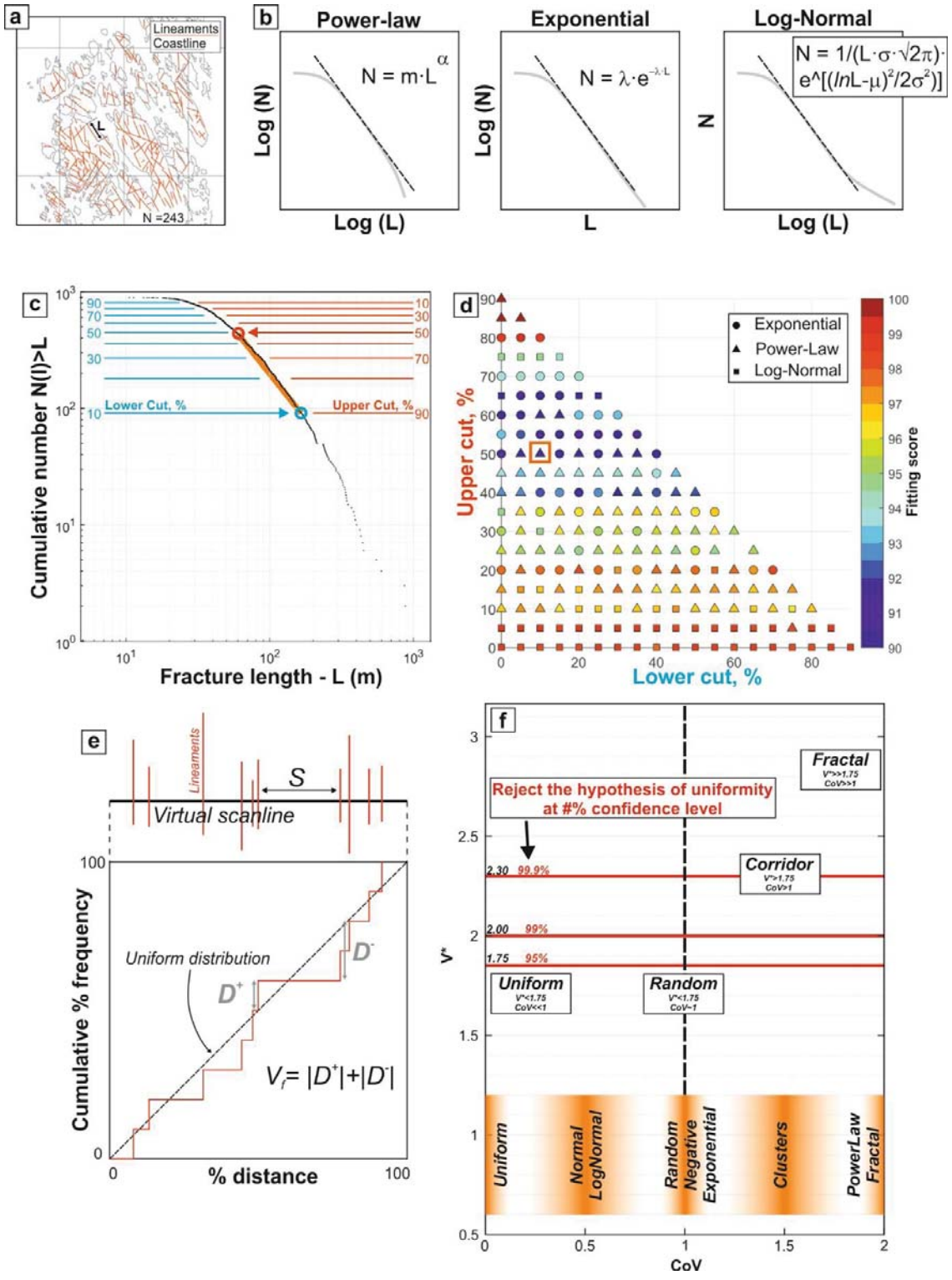

306 **Figure 2.**

307 Explanatory figure supporting the Method section. (a) Example of lineament map retrieved from the
308 analysis of small scale DTMs. (b) Schematic representation of power-law, negative exponential and
309 log-normal distributions, each of which defines a linear relationship between length L and
310 cumulative number N on a log-log, linear-log or log-linear diagram, respectively. (c) Example of
311 cumulative length distribution, plotted on a log-log diagram, obtained from the analysis of
312 lineament maps explaining graphically what the upper cut and lower cut values are. The blue and
313 red circles represent the upper and lower cut values related to the checkerboard in (d). The orange
314 segment represents the sub-domain of the cumulative distribution, included between the upper cut
315 and lower cut bounds, fitted by the power-law relation identified by MLE-KS tests. (c) Example of
316 checkerboard diagram. Each symbol (circle, triangle, square) represents a different fitting function,
317 and each symbol is color-coded according to the fitting score yielded by the MLE-KS test for the
318 portion of the cumulative distribution delimited by upper and lower cut values (plotted on the Y-
319 and X-axis, respectively). The orange square represents the results of the MLE-KS tests performed
320 on the distribution subdomain shown in (c). (e) Schematic representation of a virtual scanline and
321 the related diagram showing the difference (D values) between the observed lineament distribution
322 and a theoretical uniform (constant) distribution of spacings. (f) CoV-V* diagram showing the
323 expected ranges for uniform, random, clustered and fractal spacing distributions.

324

325

4. Results

4.1. Lineament maps description

The manual picking of topographic lineaments on different digital representations of Bømlo led to the production of lineament maps with the spatial distribution and organization of topographic lineaments at different scales (Fig. 3). The orthophotos retrieved from UAV-drone surveys and the related lineament map (Fig. 3a) help characterize the main outcrop of the Goddo Fault Zone along the eastern shoreline of the island of Goddo (Ceccato, Viola, Antonellini, et al., 2021; Ceccato, Viola, Tartaglia, et al., 2021; Viola et al., 2016). Even though the number of lineaments interpreted from UAV-drone imagery is statistically significant (n=930), the N-S- trending outcrop exposure, its 3D topography and the location of the exposed area along a major fault zone question whether the obtained results may be truly representative of the larger-scale fracture network. Lineament mapping on LiDAR DTM and aerial imagery at 1:5,000 scale (Fig. 3b) was thus performed on the best exposed areas along the coastline of the Goddo Island and the nearby smaller islands. The resulting lineament map covers more than 17 km^2 and includes n=3,835 interpreted lineaments. Furthermore, we generated additional lineament maps from the interpretation of the LiDAR DTM at the 1:25,000 and 1:100,000 scales, which cover the same area (83 km^2; Fig. 3c-d). The 1:25,000 lineament map contains n=894 lineaments, whereas the 1:100,000 map contains n=249 lineaments.

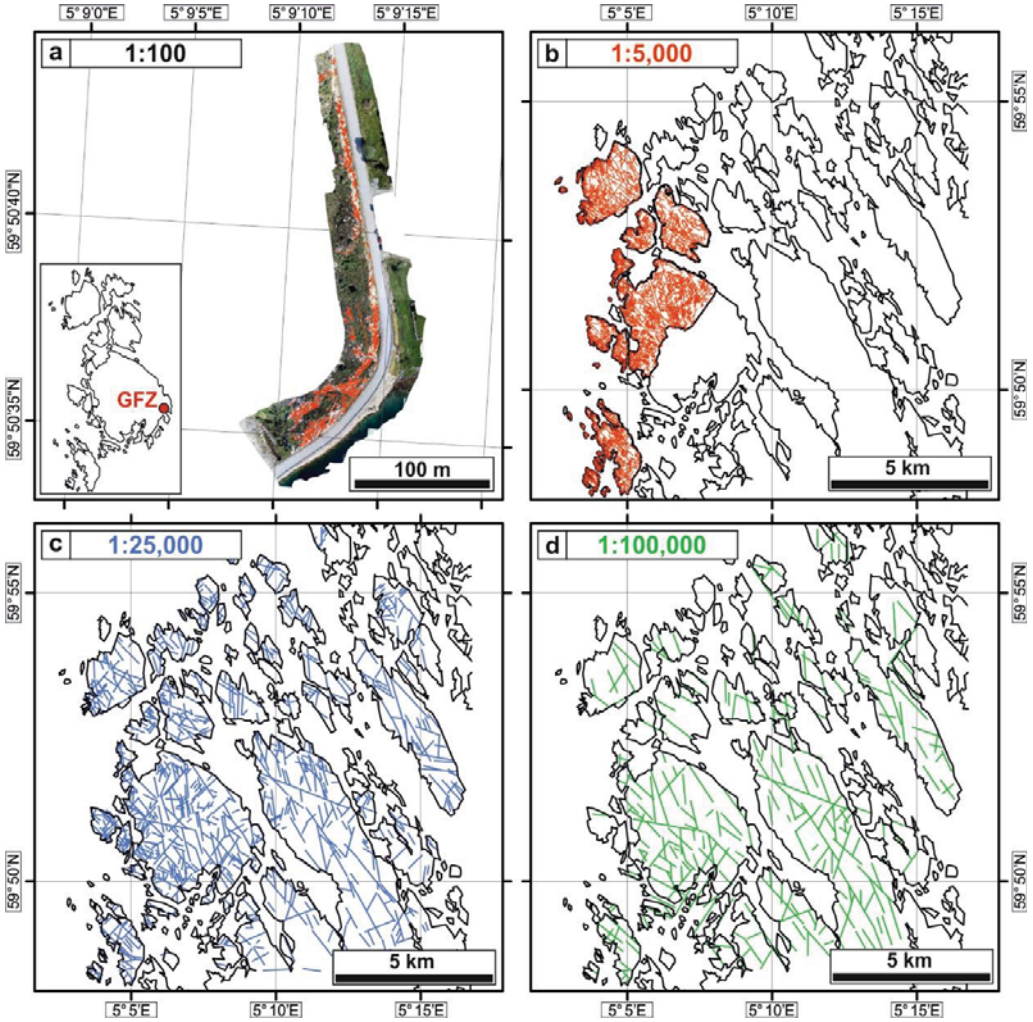

Figure 3.

Lineament Maps retrieved from the manual lineament picking on outcrop orthophotos (a) and DTM from LiDAR surveys (b-c-d).

350 *4.2. Fractal dimension*

351 The fractal dimension of the lineament maps at all scales was evaluated by applying the box-
352 counting method (Bonnet et al., 2001; Gillespie et al., 1993) (Fig. 3). The number of filled boxes
353 decreases with increasing box size following a power-law relationship (Fig. 4). The power-law
354 exponents (the fractal exponent D) retrieved from the box counting analyses of the lineament maps
355 at different scales ranges between 1.45 and 1.61 (Fig. 4). On average, the fracture network is
356 characterized by a fractal dimension D = 1.51± 0.14 (2σ).

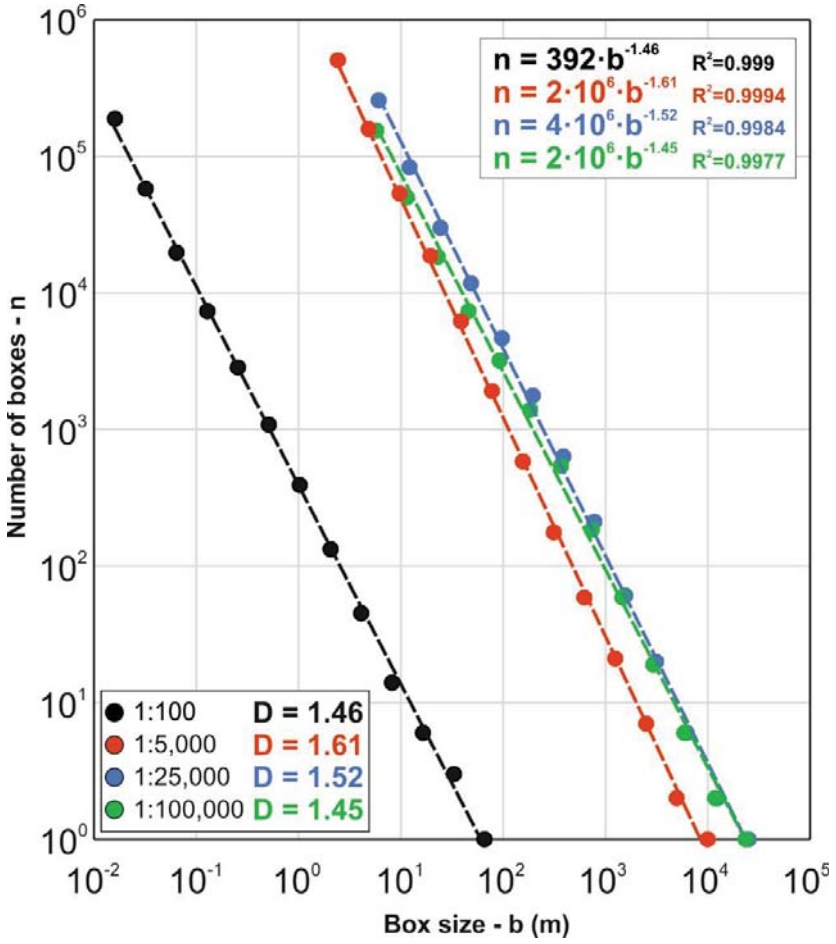

357

358 **Figure 4.**

359 Results of the box-counting method applied to the lineament maps of Fig. 3.

360

4.3. Orientation

The comparison of the rose diagrams at different scales of observation makes it possible to define some dominant orientation trends in the study area (Fig. 5a-b). The five main identified orientation trends are (Fig. 5a, Supplement S1, Table 1): (a) a N-S-striking Set 1; (b) a NE-SW-striking Set 2; (c) a ENE-WSW-striking Set 3; (d) a ESE-WNW-striking Set 4, and (e) a SE-NW-striking Set 5. These sets display a significant variation of their relative abundance across the scales. At the smallest scale of observation (1:100,000), Set 5 is dominant, whereas at the largest observation scale (1:100), Sets 1 and 2 are dominant (Fig. 5b). At intermediate scales (1:5,000; 1:25,000), all sets are equally represented (Table 1). Set 3 is the least represented, occurring in only small percentages (<10%) at all scales (Table 1). Sets 2 to 5 have a constant average orientation across all scales but Set 1 lineaments have a variable average orientation with scale. Average N-S-striking orientations are dominant at the smallest and largest scales of observation. At the intermediate scale, Set 1 presents either a NNW- (scale 1:5,000) or a NNE dominant strike (scale 1:25,000) (Fig. 5a). Therefore, we have subdivided Set 1 into Set 1a, including NNE-SSW-striking lineaments, and Set 1b, including N-S- to NNW-SSE-striking lineaments. This subdivision will be mainly adopted for the analysis of the spatial organization of the lineaments.

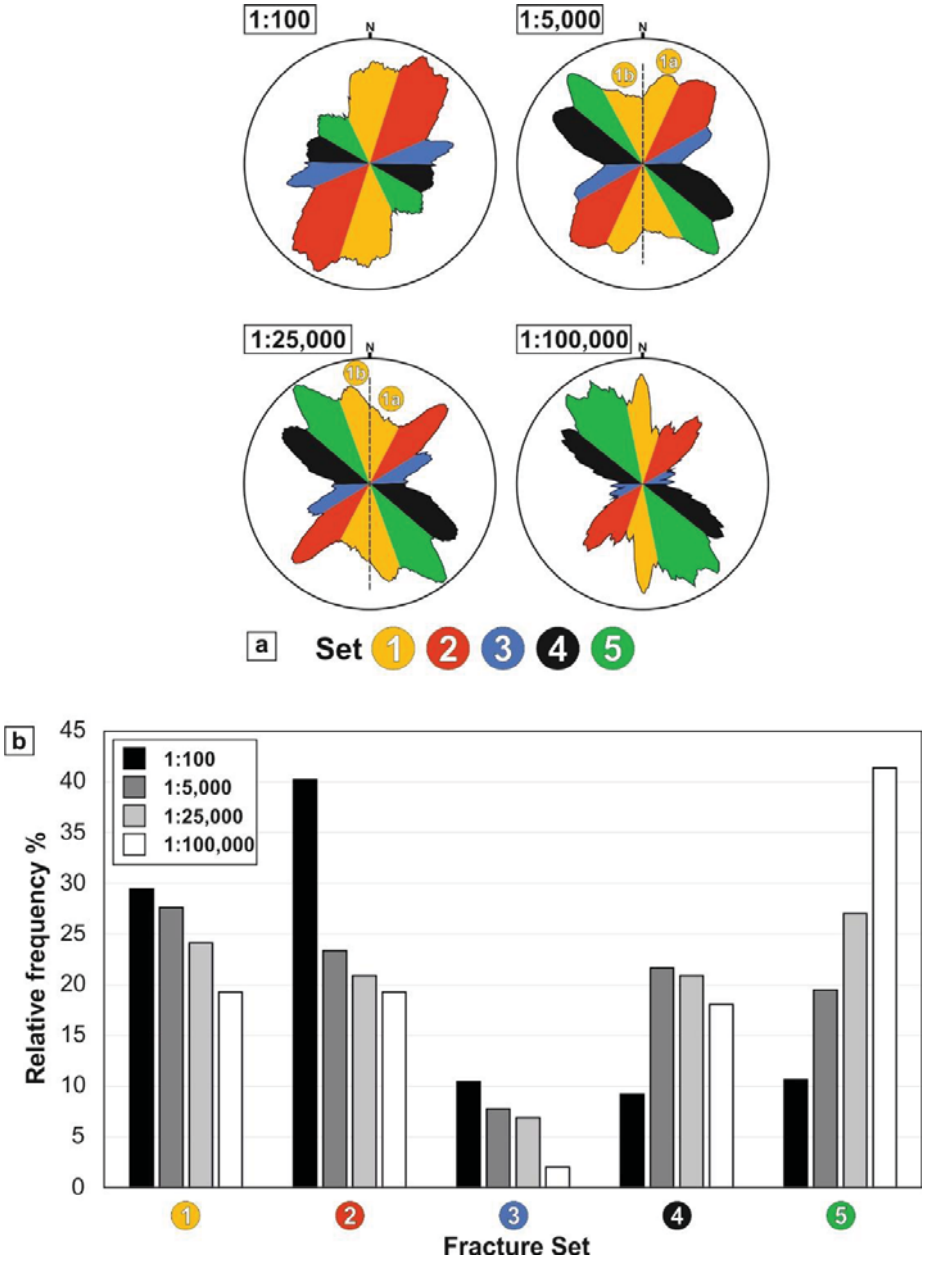

Figure 5.

Rose diagrams (a) and histograms of the relative frequencies (b) of the identified orientation sets at different scales of observation.

	Set	Azimuth (°)	N	Relative frequency (%)	Avg P_{20} (m^{-2})	Total Length (m)	Avg P_{21} (m/m^2)
Scale	**1:100**						
Area (m^2)	**1**	0-17; 156-180	274	29.46	0.1288	490.1	0.2304
2127	**2**	19-67	374	40.22	0.1758	771.86	0.3629
	3	68-91	97	10.43	0.0456	156.25	0.0735
	4	92-120	86	9.25	0.0404	134.12	0.0631
	5	121-155	99	10.65	0.0465	175.3	0.0824
	Total		930		0.4372	1727.63	0.8122
Scale	**1:5,000**						
Area (m^2)	**1**	0-28; 154-180	1059	27.61	6.16754E-05	103655.02	0.0060
17170533	**2**	29-60	896	23.36	5.21824E-05	76172.72	0.0044
	3	61-88	299	7.80	1.74136E-05	23934.34	0.0014
	4	89-130	832	21.69	4.84551E-05	80080.14	0.0047
	5	131-153	749	19.53	4.36212E-05	90759.34	0.0053
	Total		3835		0.000223348	374601.56	0.0218
Scale	**1:25,000**						
Area (m^2)	**1**	0-25; 162-180	216	24.16	2.60239E-06	93912.71	0.0011
83000724	**2**	26-59	187	20.92	2.25299E-06	60252.45	0.0007
	3	60-90	62	6.94	7.46981E-07	20544.88	0.0002
	4	91-131	187	20.92	2.25299E-06	74024.49	0.0009
	5	131-161	242	27.07	2.91564E-06	113476.26	0.0014
	Total		894		1.0771E-05	362210.79	0.0044
Scale	**1:100,000**						
Area (m^2)	**1**	0-19; 171-180	48	19.28	5.78308E-07	35972.83	0.0004
83000724	**2**	20-60	48	19.28	5.78308E-07	38877.02	0.0005
	3	61-90	5	2.01	6.02404E-08	4354.5	0.0001
	4	91-130	45	18.07	5.42164E-07	36742.25	0.0004
	5	131-171	103	41.37	1.24095E-06	106590.06	0.0013
	Total		249		2.99997E-06	222536.66	0.0027

Table 1.

Table presenting the orientation data for the identified lineament sets for each scale of observation.

4.4. Cumulative length distributions

We have analyzed the length probability distribution function of (i) all lineaments included in each lineament map at different scales (Fig. 6a) and (ii) each lineament set at different scales (Fig. 6b). We have performed the MLE-KS statistical tests for each set at different scales and the cumulative distribution at each scale to define the best fitting function for each probability distribution (Table 2). The results of MLE-KS tests are reported and summarized in Table 2; the checkerboards diagrams are reported in the supplementary material (Fig. Supplement S2).

We present in Table 2 the range of upper cut values for which each function fits best: the upper cut values quantify the "truncation" of the cumulative distribution at short lengths, and this has been demonstrated to deeply affect the results of MLE-KS tests (Dichiarante et al., 2020). Where possible, we have also considered the minimum number of fractures to retrieve a statistically significant distribution (number of lineaments >200; red lines in Fig. Supplement S2) (Bonnet et al., 2001).

The results of the MLE-KS tests suggest that a log-normal function best approximates the entire probability distribution in all considered cases (Fig. Supplement S2; Table 2). Variably truncated distributions are best approximated by either negative exponential or power-law functions (Table 2). In particular, the truncated length probability distributions for both single sets and the entire lineament network mapped at the large scale (1:100) of the GNF outcrop are best represented by negative exponential functions, with λ ranging between 0.65 and 1.25. Truncated distributions retrieved from lineament maps at 1:5,000 are best fitted, in most cases, by power-law functions with a minimum exponent α of 2.2. The truncated distributions of Sets 3 and 4 mapped at 1:5,000 can be described by both negative exponential and power-law functions. Truncated length distributions for lineaments mapped at 1:25,000 and 1:100,000 scale are well approximated by negative exponential functions, with an average λ of 0.004 and 0.0017, respectively (Table 2).

Figure 6a reports the cumulative length distributions for the entire set of lineament maps normalized to the area of investigation at each scale of observation. Even though each cumulative distribution is best approximated by either power-law or exponential (or log-normal) functions (Table 2), all the plotted normalized cumulative distributions seem to obey a general power-law relationship valid over five orders of magnitude (1 m to 10,000 m). The power-law exponent α is -1.95 (Fig. 6a). Figure 6b reports the cumulative length distributions for each set of lineaments mapped at different scales and normalized for the area of investigation. Also in this case, all the plotted distributions obey a general power law scaling with a characteristic exponent α for each set of lineaments (Fig. 6b, Supplement S3). The exponent α ranges between -1.68 and -2.2. The cumulative distributions for Set 4 lineaments mapped at the 1:5,000, 1:25,000 and 1:100,000 scale are approximated well by a general power-law function with an average exponent α = -2.2. Set 4 lineaments at the 1:100 scale, however, do not plot along this general power-law trend (Fig. 6b, Supplement S3).

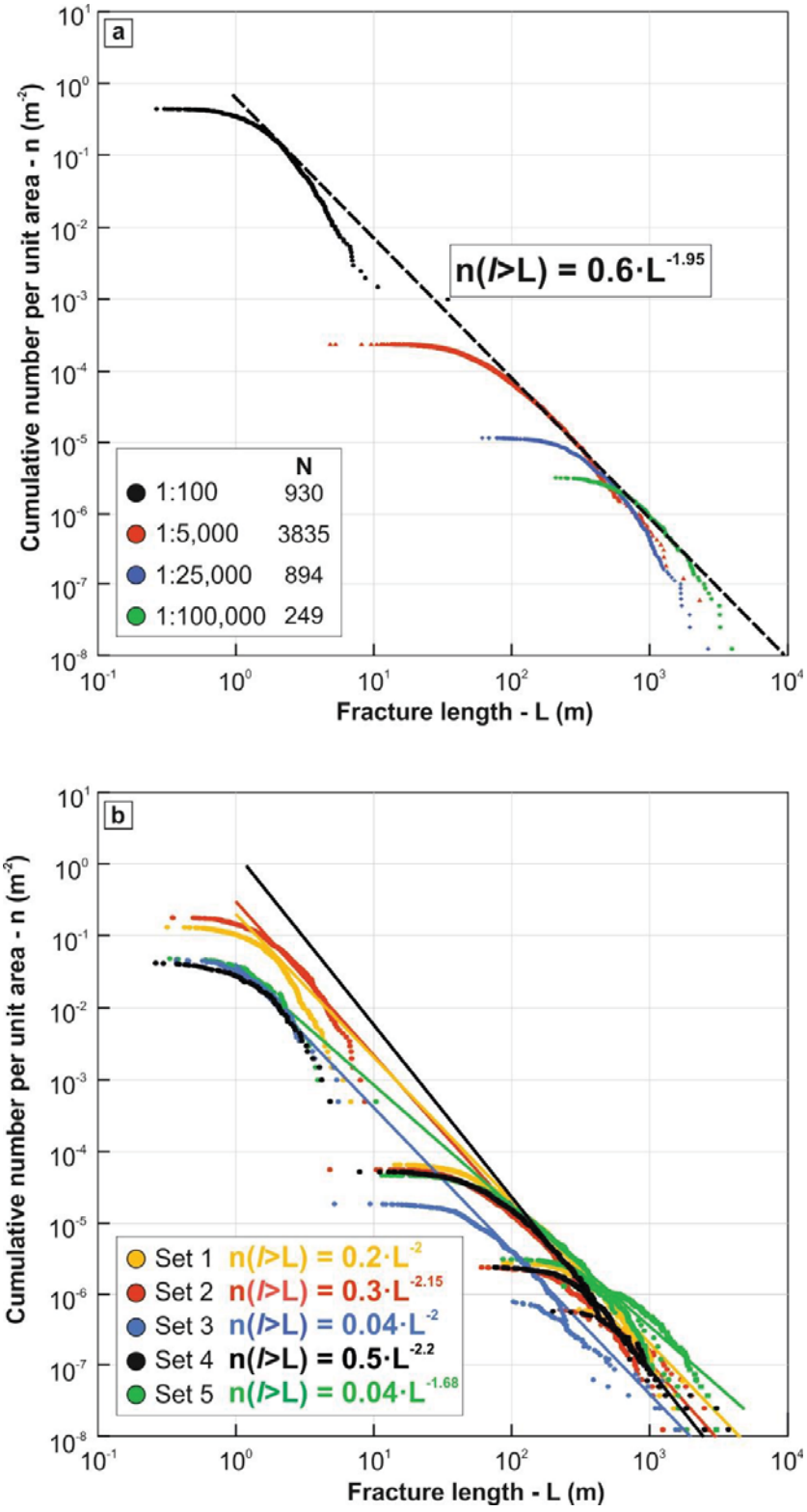
a
Cumulative number per unit area - n (m-2)
Fracture length - L (m)
n(/>L) = 0.6·L-1.95
N
1:100 930
1:5,000 3835
1:25,000 894
1:100,000 249
b
Cumulative number per unit area - n (m-2)
Fracture length - L (m)
Set 1 n(/>L) = 0.2·L-2
Set 2 n(/>L) = 0.3·L-2.15
Set 3 n(/>L) = 0.04·L-2
Set 4 n(/>L) = 0.5·L-2.2
Set 5 n(/>L) = 0.04·L-1.68

424

425 **Figure 6.**

426 (a) Log-log diagram showing the cumulative length distribution for the whole lineament maps
427 reported in Fig. 3, normalized by the investigated area. (b) Log-log diagram showing the cumulative
428 length distribution for each orientation set.

429

430

							Exponential				Power-law				Log-Normal			
Scale	Set	n	Length min (m)	Length max (m)	Avg Length (m)	Fitting Score	Range (UC %)	λ	Xmin (m)	Fitting Score	Range (UC %)	α	Xmin (m)	Fitting Score	Range (UC %)	μ	σ
1:100	1	274	0.3	6.9	1.8	>90	40-90	1.05-1.25	>1.4	-	-	-	-	>90	0-35	0.45-0.75	0.52-0.37
	2	374	0.3	8.7	2.1	>90	>10	0.65-0.79	>0.9	-	-	-	-	>90	0-5	0.55-0.65	0.55-0.57
	3	95	0.4	5.6	1.6	>90	10-65	0.95-1.05	0.8-1.8	>90	70-85	3.8-5	1.9	>90	0-5	0.35-0.45	0.5-0.55
	4	86	0.3	5.0	1.6	>90	>50	1.05-1.25	>1.25	-	-	-	-	>90	0-45	0.25-0.75	0.35-0.65
	5	99	0.3	10.7	1.8	>90	15-65	0.90-1.05	0.9-2.0	>90	>70	4.25-4.75	2.1	>90	0-10	0.4-0.5	0.46-0.55
	Total	930	0.3	10.7	1.9	>90	15-60	0.78-0.82	1.2-2.0	>90	>65	3.6-4.1	2.1	>90	0-10	0.45-0.65	0.51-0.59
1:5,000	1	1059	14.4	1759.3	97.9	<90	15-20	0.013	40-50	>90	>25	2.2-3.1	50	<90	0-10	4.3-4.5	0.63-0.72
	2	896	4.8	1315.6	85.0	<90	10-20	0.016	40	>90	>25	2.4-3.2	50	<90	0-5	4.25	0.67-0.70
	3	299	5.3	1265.5	80.0	<90	10-20; 40-55	0.017; 0.015	40; 60	<90	25-35; >60	2.6; 2.8-3.4	50; >60	>90	0-5	4.2	0.65-0.7
	4	832	8.1	1014.3	96.3	<90	10-40; 55-65	0.013; 0.0115	45; 80	<90	45-55; >70	2.6; 2.9	50; 90	>90	0-5	4.3	0.7
	5	749	11.8	2306.4	121.2	<90	25	0.01	60	<90	>30	2.4-2.8	70	<90	0-20	4.5-4.8	0.65-0.77
	Total	3791	4.8	2306.4	97.9	-	-	-	-	<90	>45	2.4-3.2	70	<90	0-40	4.3-4.7	0.55-0.75
1:25,000	1	216	88.7	1681.5	434.8	>90	>5	0.0036-0.0043	200	-	-	-	-	>90	0-5	5.5-6	0.45-0.55
	2	187	61.2	1264.1	322.2	>90	>10	0.0045-0.0052	175	-	-	-	-	>90	0-5	5.6-5.7	0.54-0.57
	3	62	105.0	1678.7	331.4	>90	0-10; >75	0.0045; 0.003	125; 275	>90	15-70	2.6-2.9	150	-	-	-	-
	4	187	79.0	2652.4	395.9	>90	10-70	0.0038-0.004	200-400	>90	>75	3.6-3.8	425	>90	0-5	5.8-5.9	0.55-0.57
	5	242	89.9	1946.3	468.9	>90	5-75	0.0032-0.0037	250	>90	>80	3.8-4.6	600	>90	0	6	0.55
	Total	894	61.2	2652.4	405.2	>90	>10	0.0034-0.004	200	-	-	-	-	>90	0-5	5.8-6	0.55-0.57
1:100,000	1	48	312.5	1892.8	749.4	>90	>35	0.0029-0.0034	650	-	-	-	-	>90	0-30	6.5-6.7	0.34-0.41
	2	48	226.2	2683.6	809.9	>90	0-15; 30-90	0.0016-0.0019	300	-	-	-	-	>90	20-25	6.7	0.5
	3	5	400.4	1586.0	870.9	-	-	-	-	-	-	-	-	-	-	-	-
	4	45	208.5	3936.9	816.5	-	-	-	-	-	-	-	-	-	-	-	-
	5	103	250.0	3224.7	1034.9	>90	>15	0.0016-0.0018	300	-	-	-	-	>90	0-10	6.8-6.9	0.47-0.55
	Total	249	208.5	3936.9	893.7	>90	>10	0.0017-0.00185	400	-	-	-	-	>90	0-5	6.7-6.8	0.5-0.55

Table 2.

Summary table of the results of MLE-KS statistical tests on distribution fitting. The results showing the highest fitting score from MLE-KS tests are indicated by a grey background.

4.5. Lineament density and intensity

As also suggested by the variation of the relative proportions of the dominant orientation sets across the scales (Fig. 5a-b), also the normalized density P_{20} (m^{-2}) and intensity P_{21} (m/m^2) of each fracture set vary across scales. The variations of density and intensity are both described by a power-law relationship in log-log diagrams plotting the scale on the X-axis (e.g., 10^5 = 1:100,000) and the density P_{20} or intensity P_{21} on the Y-axis (Fig. 7a-b) (e.g., Castaing et al., 1996). The variation trend for the total lineament density P_{20} of each map at different scales is characterized by power-law exponents β = -1.77, which also corresponds to the average of the exponent values of all the other lineament sets (Fig. 7a). Sets 1, 2 and 3 display β values larger than the average value; Sets 4 and 5 display β values smaller than the average values. Similarly, the variation trend for P_{21} is characterized by a power-law exponent δ = -0.86 (Fig. 7b); Sets 1, 2 and 3 show values of δ larger than the average value. Sets 4 and 5 display δ values smaller than the average value.

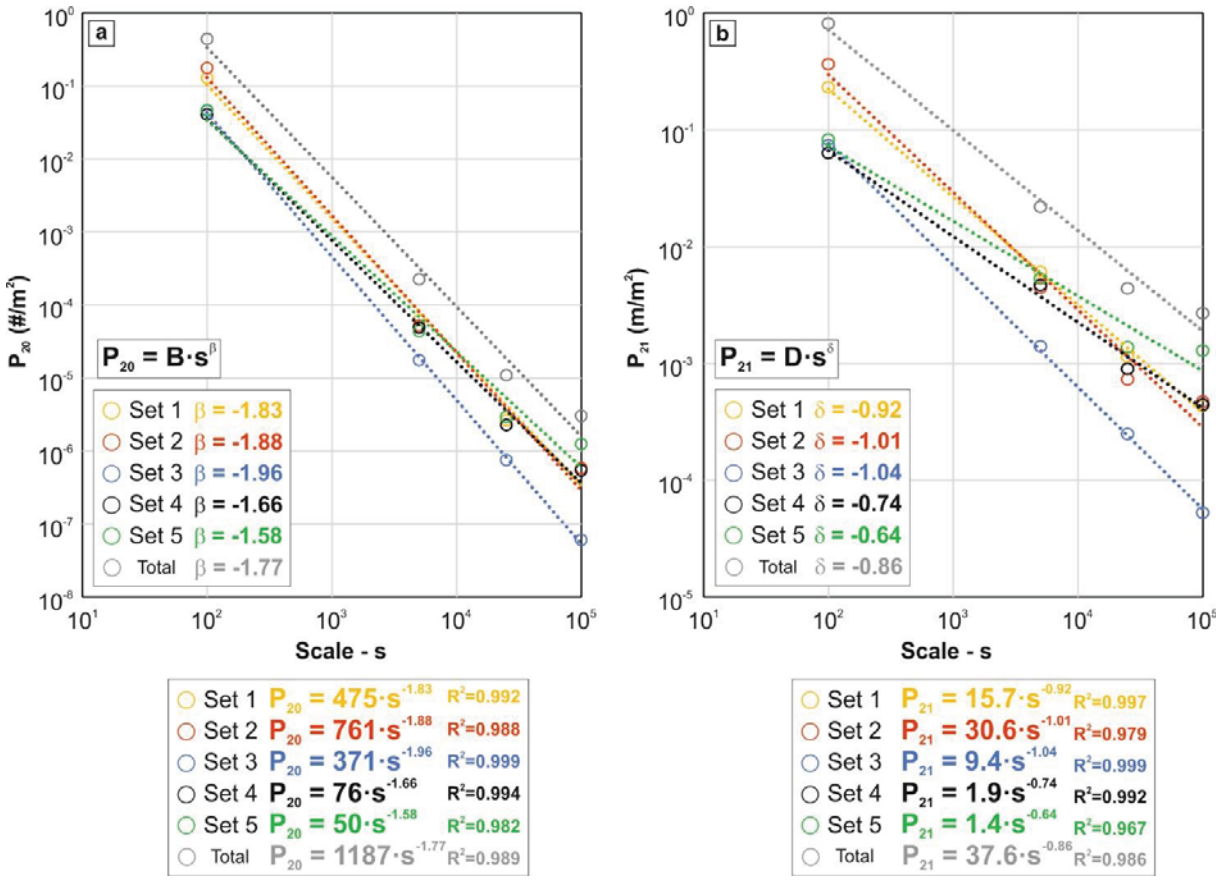

448 **Figure 7.**

449 Lineament density (P_{20}) and intensity (P_{21}) variation across scales of each orientation set.

450

4.6. Spacing and organization at different scales

The spatial organization of fracture sets has been qualitatively estimated by comparing the values of the heterogeneity parameter V_f, its statistical significance level V* and the Coefficient of Variation CoV for the scanlines performed in NetworkGT (Fig. 8; Table 3). At the 1:5,000 scale (Fig. 8a), scanlines intersecting both Set 1a and 1b lineaments are characterized by CoV ≤ 1 and V* < 1.75. This suggests that Set 1 may express a random-to-uniform spatial distribution. The same is observed at smaller scales (Fig. 8b-c), where CoV for Set 1 decreases on average, suggesting an even more random-to-uniform distribution. Set 2 lineaments display CoV on average >1 at the 1:5,000 scale, and V* >1.75 for more than half of the observed values. This might suggest that Set 2 lineaments are characterized by a clustered spatial distribution at the 1:5,000 scale. At smaller scales, both CoV and V* values generally decrease, although some of the analyzed scanlines still display CoV >1 and V* >1.75-2.00. Set 3 lineaments are too scattered and sparce to allow for a meaningful analysis of their spatial arrangement and, therefore, they are not reported in Fig. 8. Set 4 lineaments mapped at the 1:5,000 scale on average show CoV values >1, but V* is rarely >1.75. At smaller scales, both CoV and V* decrease progressively. CoV and V* for Set 5 lineaments are generally <1 and <1.75, respectively, at each scale of observation.

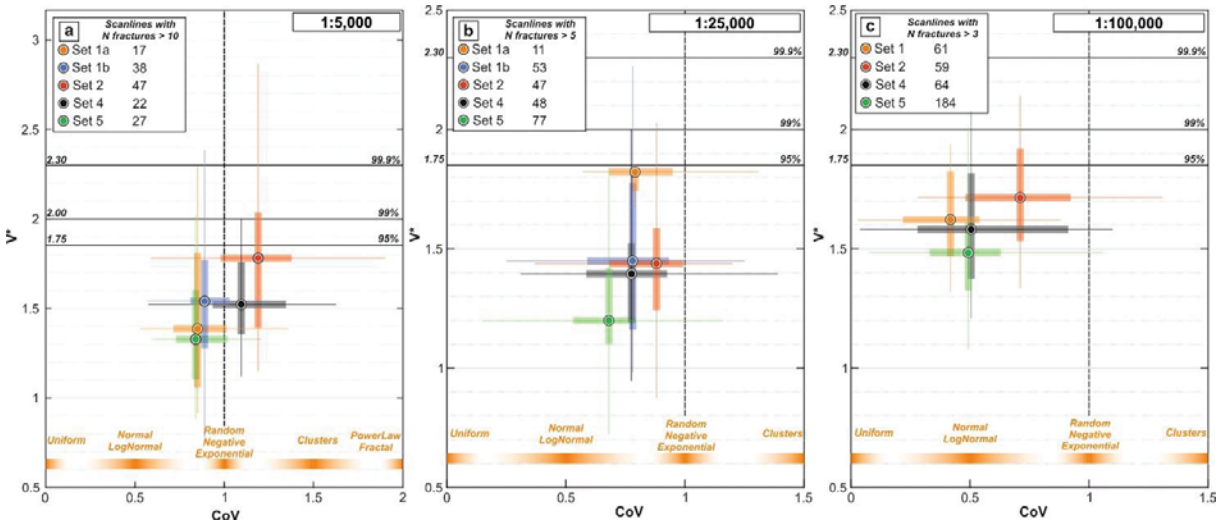

469 **Figure 8.**

470 CoV-V* spatial organization diagrams for the orientation sets identified in the lineament map at (a)

471 1:5,000; (b) 1:25,000; and (c) 1:100,000 scale.

	Scale	1:5,000			1:25,000			1:100,000		
	Set	Spacing (m)	CoV	V*	Spacing (m)	CoV	V*	Spacing (m)	CoV	V*
		N>10: 17			N>5: 59			N>3: 61		
Avg	1a	132.64	0.91	1.45	622.20	0.80	1.64	738.25	0.42	1.40
Std dev		78.55	0.28	0.43	394.10	0.27	0.27	314.96	0.22	0.21
Min		19.37	0.53	0.92	52.09	0.24	1.07	262.68	0.03	1.03
Max		232.39	1.69	2.30	1568.75	1.42	2.01	1253.90	0.88	1.80
		N>10: 38			N>5: 106			-		
Avg	1b	189.33	0.93	1.55	487.49	0.68	1.49	-	-	-
Std dev		52.19	0.18	0.37	175.44	0.26	0.35	-	-	-
Min		87.87	0.57	0.78	133.91	0.12	0.98	-	-	-
Max		311.72	1.44	2.38	883.45	1.25	2.26	-	-	-
		N>10: 47			N>5: 122			N>3: 59		
Avg	2	133.39	1.21	1.78	637.66	0.71	1.50	1013.41	0.71	1.52
Std dev		45.48	0.32	0.44	512.73	0.27	0.27	304.75	0.28	0.27
Min		37.64	0.59	1.15	89.24	0.09	0.87	352.64	0.28	1.05
Max		213.61	2.02	2.87	2195.76	1.26	2.12	1506.44	1.31	2.05
		N>10: 22			N>5: 150			N>3: 64		
Avg	4	135.66	1.10	1.54	403.84	0.69	1.44	671.34	0.50	1.34
Std dev		41.33	0.29	0.27	238.35	0.23	0.27	403.20	0.26	0.28
Min		75.78	0.57	1.12	72.51	0.22	0.82	150.10	0.04	0.89
Max		251.38	1.62	2.00	1013.70	1.51	2.01	1566.48	1.10	1.96
		N>10: 27			N>5: 261			N>3: 184		
Avg	5	150.88	0.89	1.36	404.46	0.58	1.36	453.89	0.49	1.23
Std dev		69.94	0.23	0.31	219.18	0.25	0.26	174.28	0.22	0.26
Min		51.16	0.60	0.88	83.31	0.08	0.72	52.05	0.08	0.72
Max		255.16	1.62	2.02	1005.32	1.24	2.07	963.48	1.06	1.88

472

473 **Table 3.**

474 Spacing, CoV and V* statistical parameters.

475

476

5. Discussion

In the following, we firstly assess the scaling laws and exponent values obtained for the Bømlo fracture network as well as their implications upon the classification of lineaments as geological structures (e.g., fracture and fault zones). Then, we discuss the implications related to applying the retrieved scaling relationships to the quantification of fracturing and reservoir permeability at different scales. In addition, we evaluate the possible causes behind the observed discrepancy between the results of multiscale and single-scale parameter quantifications.

5.1. Characterization of geometric properties of the Bømlo fracture network

The fractal dimensions D retrieved from the analysis of 2D lineament maps cluster around 1.5 (Fig. 4), similar to what is commonly reported from other case studies on fracture pattern fractal dimensions (Bonnet et al., 2001; Hirata, 1989). Also, the normalized cumulative distribution of fracture lengths effectively defines a single scaling law, which can be best described by a power-law relationship with an exponent α = -1.95 (Fig. 6a; Table 4). The general scaling law obtained for the overall fracture network is very similar to that derived from many other case studies of fracture networks affecting both crystalline basements and (meta)sedimentary rocks, with an average power-law exponent very close to α = -2 (cf. Bertrand et al., 2015; Bonnet et al., 2001; Bossennec et al., 2021; Chabani et al., 2021; Le Garzic et al., 2011; McCaffrey et al., 2020; Odling, 1997; Torabi & Berg, 2011). Similarly, the power-law scaling relationship defined by the fracture density P_{20} values is characterized by a power-law exponent β = -1.77, similar to the value of -1.7 commonly observed in many other fault networks (Castaing et al., 1996; Bonnet et al., 2001, and references therein).

These two features (similar fractal dimension and power-law scaling relationship) are commonly used as evidence for the occurrence of a fracture network whose geometrical properties (size of fractures, i.e., length, and spatial correlation and organization) are scale-invariant (Bonnet et al., 2001). This suggests that, at a first approximation, the documented fracture pattern in the crystalline basement of Bømlo is self-similar at any scale of observation. However, the Bømlo case may be

more complex than it would seem at a first glance. The Bømlo fracture network is composed of five main orientation sets with variable relative abundance, density and intensity across scales (Figs. 5 and 7, Table 1). The observed variations of density and intensity are predictable and can be described by a general power-law scaling, the exponent of which is characteristic of each orientation set (Fig. 7; Table 4). Even though the cumulative length distribution for each orientation set at each observation scale can be best approximated by other scaling laws than power-law (Table 2), the cumulative length distribution across scale is best approximated by a power-law scaling relationship (Fig. 5b; Table 4). Again, each orientation set is characterized by its own power-law exponent (Fig. 5b; Table 4), which differs slightly from that computed for the entire fracture network.

These variations of density and intensity of orientation sets across scales could be related to changes in resolution of the digital representation of the terrain (DTMs and orthophotos) with a changing scale of observation (Scheiber et al., 2015). However, conversely to what reported here, the change in resolution would affect each orientation set equally, thus maintaining a constant relative abundance across scales. Another possible bias affecting the identification of fractures at different scales may result from the constant direction of the light source adopted for the LiDAR DTM hillshading (light source from NW in this case). Likely, this may affect the detection of lineaments at specific orientations, but systematic effects have not been identified by previous studies (Scheiber et al., 2015).

Nevertheless, some fracture sets clearly display similar trends of variation of the relative abundance and intensity, such that they can be grouped into two main set types (Fig. 9; Table 4): (1) Type A includes Sets 1, 2 and 3, characterized by comparable P_{20} and P_{21} variation trends across scales, with similar β and δ exponents close to -1.90 and -0.95, respectively – their relative abundance decreases from 1:100 to 1:100,000 scale (Fig. 9a-b); (2) Type B includes Sets 4 and 5, with a comparable variation trend in intensity, characterized by $\beta \approx$ -1.60 and $\delta \approx$ -0.70, and a similar

variation of the relative abundance across scales, showing an increasing fracture intensity from 1:100 to 1:100,000 scale (Fig. 9a-b). The sorting into Type A and B is also justified by the power-law exponents of the general cumulative length distribution for each fracture set (Figs. 6b, 9c; Table 4). Type A fracture sets are characterized by a power-law exponent α close to -2 or smaller. Type B fracture sets, instead, are characterized by power-law exponents >-2. Whereas this is true for Set 5 (α = -1.68), it is rather difficult to find a general power-law relation that encompasses the entire set of scales of observation for Set 4 (see Fig. Supplement S3). The cumulative length distributions also show that the longest lineaments, those of likely regional significance observed at small scale (1:25,000, 1:100,000), belong to Type B sets.

This classification into Type A and B fracture sets is not directly reflected in the CoV-V* diagrams that quantify the spatial organization of fracture sets (Fig. 8a-b). Conversely to all the other analyzed parameters, even though the fracture network as a whole presents scale-invariant geometrical features as suggested by the rather constant fractal dimension D, the spatial organization of its constituent components, that is, the individual fracture sets, seems to be scale-dependent. As a consequence, we can infer that the spacing distribution of fractures belonging to each fracture set is scale-dependent. The CoV-V* diagrams highlight a similar decreasing trend for all the analyzed fracture sets with increasing scale of observation (from 1:100,000 to 1:5,000). The most significative variation across scales in the spatial distribution occurs for Set 2 and Set 4, both of which exhibit a tendency to occur as clusters at the large scale (1:5,000; CoV > 1, V* > 1.75; Figs. 8a-9d), whereas they are randomly-to-uniformly distributed at the smaller scales (1:25,000 and 1:100,000; CoV < 1; V* < 1.75; Figs. 8b-c, 9e). Set 1 (a & b) and Set 5 are randomly-to-uniformly distributed at all scales of observations (CoV < 1; V* < 1.75; Figs. 8, 9d-e). None of the analyzed fracture sets show a tendency to develop fractal behavior with a power-law spacing distribution. Therefore, the analyzed fracture sets appear to display a hierarchical organization within a fracture network presenting overall scale-invariant geometrical properties (e.g., Le Garzic

et al., 2011). In it, Type B lineaments represent the higher-order structures, controlling the geometrical properties of the network at the regional scale (Fig. 9d-e). The schematic representation of lineaments in Fig. 9 highlights an heterogeneous distribution of Type B lineaments, which is not captured by the statistical analysis of spacing heterogeneity. Indeed, the Rolvsnes granodiorite can be subdivided into several domains of the lineament maps where either Set 4 or Set 5 fractures are predominant at the regional scale ("Set 4-5 domain" – grey and dashed transparent areas in Fig. 9d-e). On the other hand, Type A lineaments represent lower-order structures and control the geometrical properties of the network at the local-to-outcrop scale (Fig. 9d-e).

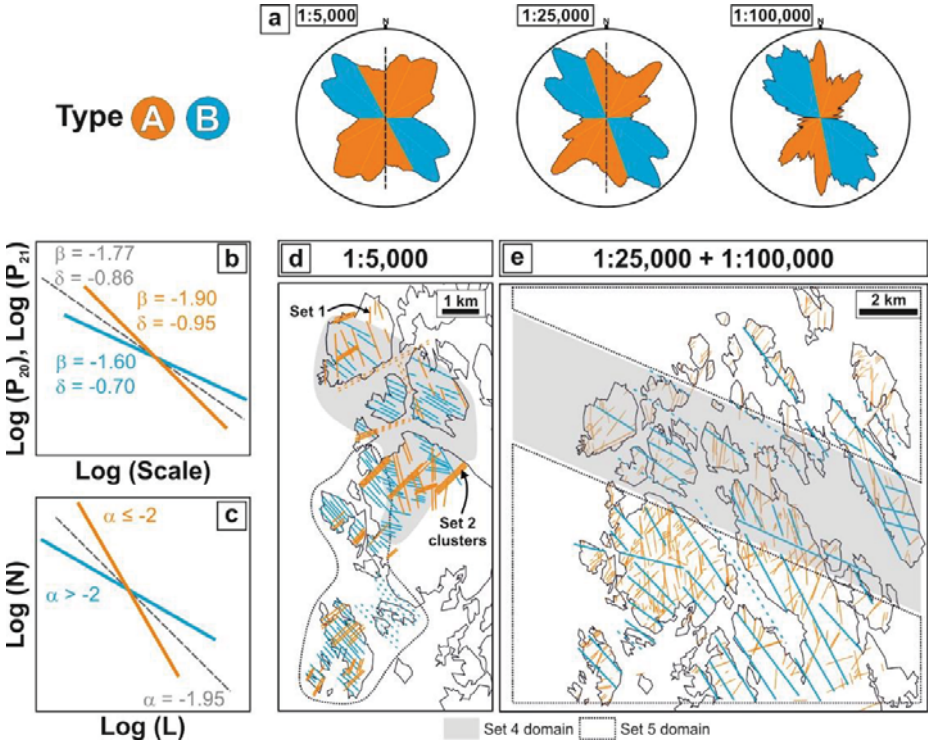

Figure 9.

Schematic summary of the results for the Bømlo case study. (a) Rose diagrams of the orientation of lineaments at different scales (1:5,000; 1:25,000; 1:100,000) with the classification into Type A and B lineaments. (b) Schematic log-log diagram showing the observed general trends of P_{20} and P_{21} variations with scale. The values of β and δ exponents are reported for the entire fracture network (grey dashed line), Type A (orange line) and Type B (light blue line) lineaments. (c) Schematic log-

567 log diagram showing the observed general scaling laws retrieved for the cumulative length
568 distributions. The values of the exponent α are reported for the entire fracture network (grey dashed
569 line), Type A (orange line) and Type B (light blue line) lineaments. (d) Schematic representation of
570 the fracture distribution at 1:5,000 scale. The reported lineament are redrawn from the 1:5,000
571 lineament map and represent the actual spatial organization observed at Bømlo. Note the clustered
572 organization of Set 2 fractures and the two domains (highlighted by transparent grey and dashed
573 areas) where Set 4 and Set 5 fractures are dominant, respectively. (e) Schematic representation of
574 the fracture distribution at 1:25,000–1:100,000 scales. The reported lineaments are redrawn from
575 the 1:25,000–1:100,000 lineament maps and represent the actual spatial organization mapped on
576 Bømlo.

577

		Cumulative length distributions		**P20 density distribution**			**P21 intensity distribution**		
		$N(l>L)= A\cdot L^{\alpha}$		**$P_{20} = B\cdot s^{\beta}$**			**$P_{21} = D\cdot s^{\delta}$**		
	Set Type	A	α	B	β	R^2	D	δ	R^2
Set 1	A	0.2	-2	475	-1.83	0.992	15.7	-0.92	0.997
Set 2	A	0.3	-2.15	761	-1.88	0.988	30.6	-1.01	0.979
Set 3	A	0.04	-2	371	-1.96	0.999	9.4	-1.04	0.999
Set 4	B	0.5	-2.2	76	-1.66	0.994	1.9	-0.74	0.992
Set 5	B	0.04	-1.68	50	-1.58	0.982	1.4	-0.64	0.967
Total		0.6	-1.95	1187	-1.77	0.989	37.6	-0.86	0.986

578

579 **Table 4.**

580 Summary table reporting the power-law scaling and the values of the related parameters retrieved
581 from the multiscale analysis of cumulative length distribution, fracture density and intensity.

582

583

5.2. General power-law scaling for the fracture network and fracture sets: implications and limitations

The fracture network exhibits some general power-law relationships describing the multiscale behavior of both length distribution (α = -1.95), fracture density P_{20} (β = -1.77) and fracture intensity P_{21} (δ = -0.86) (Table 4). These general power-law scaling laws may effectively be adopted to retrieve fracture network properties (geometrical properties and permeability) at any scale of observation. However, the adoption of a general scaling law for the geometrical properties, without taking into consideration the peculiarity of each fracture set building up the fracture network, may lead to an erroneous extrapolation of the analyzed properties. In particular, for our case study, significant deviations would occur in the upscaling/downscaling of fracture density P_{20} and intensity P_{21}. As shown in Figs. 5 and 6, fracture sets exhibit different power-law exponents, which are systematically smaller for Sets 1, 2 and 3 (Type A), and larger for Sets 4 and 5 (Type B) than the exponent of the fracture network taken as a whole. By adopting power-law exponents larger than the actual exponent of the fracture set would lead to an overestimation of the fracture network properties at larger scales. Vice-versa, adopting power-law exponents smaller than the actual exponent of the fracture set would lead to an underestimation of the density/intensity/length distribution at larger scale. In the case of the Bømlo fracture network, this overestimation/underestimation can be significant and it can reach one order of magnitude in terms of fracture intensity and density (Fig. 7).

In addition, field investigations (Ceccato, Viola, Antonellini, et al., 2021; Ceccato, Viola, Tartaglia, et al., 2021; Scheiber & Viola, 2018) have revealed the highly heterogeneous distribution of fractures at the outcrop scale. Only for some orientation sets, fractures are homogeneously distributed over the studied outcrop (e.g., Sets C-D of Ceccato et al., 2021a, corresponding to Sets 3-4 reported here). Most of the identified fracture sets at the outcrop present, instead, either a clustered spatial organization or a variable intensity over short distances (50-100 m). This

represents of course a limitation to the extrapolation of the general power-law identified in this study, and thus the lower bound for the application of the proposed power-law scaling (Bonnet et al., 2001). Similarly, the heterogeneous spatial distribution of Set 4 and 5 fractures identified at small scale of observation (Fig. 9d-e) needs to be accounted for when evaluating the upper limit of applicability of the general scaling laws defined here.

The outcrop-scale spatial heterogeneity and the overestimation/underestimation effects of applying a general power-law scaling become relevant when considering the role that different fracture sets may have in the definition of the net permeability of fractured crystalline basement. As highlighted by field studies (Ceccato, Viola, Antonellini, et al., 2021; Ceccato, Viola, Tartaglia, et al., 2021; Gabrielsen & Braathen, 2014), each fracture set may contribute differently to the bulk permeability of the fractured crystalline basement. Fracture clusters and minor normal faults may represent effective fluid pathways at the outcrop scale, which well represents the sub-seismic resolution scale (Ceccato, Viola, Tartaglia, et al., 2021; Place et al., 2016; Souque et al., 2019). On the other hand, fault zones may control fluid flow and reservoir compartmentalization at the regional scale (Holdsworth et al., 2019). Accordingly, any underestimation/overestimation of their density and their organized spatial distribution may deeply affect the accuracy of hydrological and petrophysical models of the fractured basement at the outcrop and at its sub-seismic resolution scale (Bertrand et al., 2015; Le Garzic et al., 2011).

The retrieved power-law relationship may thus effectively represent a powerful tool to enhance the prediction and visualization of SSRS structural features, which normally remain beyond the resolution offered by standard (large-scale seismic investigations) and high-resolution (local-scale surficial investigations, e.g., ground penetrating radar, electrical resistivity tomography) geophysical methods. These mathematical relationships provide the opportunity to infer the occurrence and the spatial heterogeneity of SSRS structures that are critical in controlling the permeability of fractured crystalline basement.

5.3. Interpretation of the Bømlo fracture network in the regional framework

We have shown that, as a whole, the granodioritic crystalline basement on Bømlo is characterized by a scale-invariant fracture network, composed of different fracture sets with a variable spatial organization across scales (Fig. 9). At the smallest scale, this fracture network is dominated by the homogeneously-spaced, WNW-to-NW-striking Set 4 and Set 5 lineaments (Type B; Fig. 9d-e). These lineaments are characteristic of and predominant over the whole of western and southwestern Norway onshore (Gabrielsen et al., 2002; Gabrielsen & Braathen, 2014), as well as offshore (Preiss & Adam, 2021). The general computed power-law exponent ($\alpha > -2$) suggests that long fractures represent a substantial part of the overall fracture population of Type B lineaments. This also suggests that Type B lineaments probably represent localized zones accommodating significant deformation, when compared to Type A structures (Ackermann et al., 2001). Therefore, these lineaments probably represent major fractures and normal fault zones formed and repeatedly reactivated during the prolonged brittle tectonic history of the Rolvsnes granodiorite forming the crystalline basement of Bømlo (Ceccato, Viola, Antonellini, et al., 2021; Preiss & Adam, 2021; Scheiber & Viola, 2018; Viola et al., 2016). At the largest analyzed scale, the fracture network is mainly dominated by random-to-clustered, NNW-SSE to NE-SW-striking fracture sets (Type A, Sets 1 & 2; Fig. 9d-e). These structures are mainly related to minor faults and mineralized veins (Set 2), fracture clusters and normal fault zones (Set 1) (cf. Gabrielsen and Braathen, 2014; Scheiber and Viola, 2018). Accordingly, the general power-law exponent ($\alpha < -2$) suggests that among Type A lineaments, short fractures represent a significant part of the lineament population, probably resulting from an early stage of distributed faulting and deformation accommodation (Ackermann et al., 2001).

The fractured and weathered crystalline basement of Bømlo, and in particular the Rolvsnes granodiorite, is generally considered as the onshore analogue of the crystalline basement of the Utsira High located offshore in the northern North Sea (Trice et al., 2019). Our results can,

therefore, provide invaluable insights on the geometry and spatial organization of the fractures within the crystalline basement of the fractured basement reservoir buried below the North Sea sedimentary cover (Fredin et al., 2017; Preiss & Adam, 2021). To extrapolate our results to the offshore fractured basement, however, one needs to also consider several other factors deeply affecting the development of fractures and fault zones regionally. First of all, the Utsira High and the Bømlo crystalline basement blocks resided at different structural levels during the North Sea rifting history, them being at the center and on the shoulder of the rift system, respectively (Scheiber & Viola, 2018). Thus, they may have been subject to significantly different deformation intensity and regimes (Bell et al., 2014). Accordingly, the length distribution, density, and intensity of the identified Type A and B lineaments offshore might significantly differ from those presented here. In addition, care must be taken when extrapolating and comparing these results to the regional framework. Indeed, structural inheritance, the occurrence of intra-basement structures and the lithological-mechanical anisotropy of the (poly)-metamorphic crystalline basement of southwestern Norway deeply affect the intensity and geometry of fracture networks at the local and regional scales (Fazlikhani et al., 2017; Fossen et al., 2017; Gabrielsen et al., 2018; Osagiede et al., 2020; Phillips et al., 2016; Preiss & Adam, 2021). This structural inheritance may lead to significant differences in the geometry and scaling properties of the fracture network when compared with those described for the Rolvsnes granodiorite.

5.4. Comparison between MLE-KS results and qualitative multiscale fitting (General scaling law)

MLE-KS statistical tests have already demonstrated their strength in the analysis of fault attribute distribution (Dichiarante et al., 2020; Kolyukhin & Torabi, 2013). In our case, the results of length cumulative distributions fitting with MLE-KS tests differ significantly from the general power-law qualitative relation defined by comparing multiscale cumulative distributions. Similar to what reported by Dichiarante et al. (2020), non-truncated cumulative length distributions are best fitted

by log-normal functions (see fitting scores <90 for log-normal functions in Table 2). Even when the distribution is best approximated by a power-law function (e.g., most fracture sets mapped at 1:5,000; Table 2), the values of the power-law exponents retrieved from MLE-KS tests (α >-2) differ from those obtained from the fitting of multiscale distributions (α = -1.95).

These deviations (both that from the power-law at each scale and that of the power-law exponents from the general ones) are commonly observed in almost all natural fracture networks. Remarkable deviations from a power-law scaling behavior have been previously explained as resulting from several causes: (i) analytical biases (such as truncation and censoring of lineaments interpreted from DTMs) (Manzocchi et al., 2009; Odling, 1997; Yielding et al., 1996); (ii) subdivision of long lineaments into segments (segmentation) (Ackermann et al., 2001; Cao & Lei, 2018; Scholz, 2002; Schultz et al., 2013; Xu et al., 2006); (iii) effectively different scaling properties at different scales of observation (Castaing et al., 1996; Le Garzic et al., 2011; Kruhl, 2013).

Justifying the observed deviation from power-law scaling at a specific scale of observation only by referring to truncation and censoring biases would mean that, in most cases, the dataset is in most part (>>50%) biased (see upper cut values > 65% for power-law fitting where negative exponential functions best approximate the cumulative distributions in Table 2), and thus of little use to any kind of statistically significant analysis.

Segmentation of long lineaments into shorter segments may be due to several causes, both introduced into the dataset by analytical/interpretative biases, and intrinsically related to the genetic fracture formation processes. Segmentation may result from partial exposure and cover of the fracture network, and it may decrease the power-law scaling exponent, without affecting the type of scaling-law function (Cao & Lei, 2018). Segmentation may be related to the progressive growth stages of fault/joint patterns evolving with increasing accommodated deformation and faulting maturity from a network composed of completely isolated short fractures to a network formed by a few long, single lineaments, through fracture interaction and interconnection (Ackermann et al.,

2001; Michas et al., 2015; Scholz, 2002). This has been demonstrated to affect both the shape of the mathematical function describing the length distribution (exponential vs. power-law), as well as the power-law exponent at a specific scale of observation (Schultz et al., 2013). However, this may explain the difference in scaling relationships observed during the evolution of a fracture network through time and not at different scales of observation. In addition, the subjective choice of tracing single segments composing a longer lineament as separate fractures rather than tracing a single, continuous, long lineament, may likely affect the cumulative length distributions of the fracture network. Tracing single segments would increase the number of short segments compared to longer segments, at constant P_{21} intensity, increasing the total number of traced lineaments, and thus decreasing the power-law exponent of the distribution (Xu et al., 2006). This segmentation bias may justify the fact that power-law exponents of the multiscale length distributions of each fracture set (Fig. 5b) are systematically smaller than those obtained from MLE-KS tests at 1:5,000 scale. Whether or not this sampling bias may effectively affect the mathematical shape of the cumulative distribution would deserve further investigations, which go beyond the scope of the present paper.

That fracture networks may effectively present different scaling properties at different scales of observations thus seems to be the most plausible option (Kruhl, 2013). Indeed, fault and fracture networks may present a hierarchical organization, which inherently implies scale-dependent geometrical properties and spatial distribution of lineaments (Castaing et al., 1996; Le Garzic et al., 2011). In fact, this is also consistent with the observed variation of relative abundances of orientation sets across scales: each lineament set contributes differently to the overall fracture network geometrical characters and thus the variation of the relative abundance may also lead to variations in geometrical properties (spatial organization and length distributions) at different scales (e.g., Le Garzic et al., 2011). Nevertheless, the combination of fracture sets with scale-dependent properties (e.g. spatial organization or length distribution functions) may result in a fracture

network responding to power-law scaling laws, which could be described as a fractal, scale-invariant fracture network (Bonnet et al., 2001).

6. Conclusions

The fractured crystalline basement of the Rolvsnes granodiorite on Bømlo is characterized by the occurrence of a fractal fracture network controlled by a general power-law scaling law for the distribution of fracture lengths. However, detailed orientation-dependent analyses have revealed that this first-approximation scale-invariant fracture network is composed of fracture sets, which individually exhibit a scale-dependent hierarchical spatial distribution, and parameter variation trends with the scale of observation. Different trends of intensity/density variation across scales for each orientation set have been detected, as well as different scaling laws for length distribution of each orientation set. These observations may suggest that the documented fracture network results from the summation of different geological structures (e.g., faults vs. joints, major fault zones vs. incipient minor faults), organized in a hierarchical manner and characterized by different geometrical and scale-dependent properties.

Our study allows us to draw some general conclusions about the methods of characterization of fracture network and their analysis:

- First of all, the presented multiscale analytical workflow may represent a valid option for the quantification of large, inherently incomplete (due to analytical and subjective biases) lineament datasets. The lineament maps retrieved from digital terrain and surface models of the Bømlo crystalline basement offer very large datasets, which are inherently incomplete due to partial exposure and/or incomplete sampling of lineament due to resolution or human bias (Scheiber et al., 2015). Thus a statistical approach such as that proposed in this paper is highly recommended when aiming to retrieve relevant information from datasets that, for several reasons, are only partially representative of the entire fracture network.

- Detailed orientation-dependent, multiscale analyses of the fracture network can provide the different scaling laws and geometrical properties for each constituent fracture set, which can be adopted to improve the detail and tune the accuracy of models of sub-seismic-resolution scale structural features and the associated permeability in fractured crystalline basements.
- The integration of multiscale length distribution analyses, multiscale intensity/density estimations and multiscale description of spatial organization provides useful information for the classification of topographic lineaments as different geological structures (e.g., fracture/joint corridors vs fault zones) with specific hierarchy and control on the permeability of the fractured basement.

Acknowledgments

Our research work was funded by the still ongoing BASE 2 project ("Basement fracturing and weathering onshore and offshore Norway—Genesis, age, and landscape development" – Part 2) and BASE 3 (NFR grant number 319849), a research initiative launched and steered by the Geological Survey of Norway and supported by Equinor ASA, Aker BP ASA, Lundin Energy Norway AS, Spirit Energy Norway AS, Wintershall Dea Norge, and NGU. We thank all BASE colleagues for continuous discussion and constructive inputs. Roberto Emanuele Rizzo is warmly thanked for fruitful discussions. Eric James Ryan is thanked for field support and the acquisition of UAV-drone imagery. The Authors declare they have no perceived financial conflicts of interests with respect to the results of this paper.

Data Availability

Data analyzed (shapefiles of manually picked lineaments and related geometrical properties) in the present paper are available at: ("Multiscale_lineament_analyses_dataset", Mendeley Data, V1, doi: 10.17632/4zdjpmr9jk.1).

781

References

Achtziger-Zupančič, P., Loew, S., & Mariéthoz, G. (2017). A new global database to improve predictions of permeability distribution in crystalline rocks at site scale. *Journal of Geophysical Research: Solid Earth*, *122*(5), 3513–3539. https://doi.org/10.1002/2017JB014106

Ackermann, R. V., Schlische, R. W., & Withjack, M. O. (2001). The geometric and statistical evolution of normal fault systems: an experimental study of the effects of mechanical layer thickness on scaling laws. *Journal of Structural Geology*, *23*(11), 1803–1819. https://doi.org/10.1016/S0191-8141(01)00028-1

Andrews, B., Roberts, J., Shipton, Z., Bigi, S., Tartarello, M. C., & Johnson, G. (2019). How do we see fractures? Quantifying subjective bias in fracture data collection. *Solid Earth*, *10*(2), 487–516. https://doi.org/10.5194/SE-10-487-2019

Bell, R. E., Jackson, C. A. L., Whipp, P. S., & Clements, B. (2014). Strain migration during multiphase extension: Observations from the northern North Sea. *Tectonics*, *33*(10), 1936–1963. https://doi.org/10.1002/2014TC003551

Bertrand, L., Géraud, Y., Le Garzic, E., Place, J., Diraison, M., Walter, B., & Haffen, S. (2015). A multiscale analysis of a fracture pattern in granite: A case study ofthe Tamariu granite, Catalunya, Spain. *Journal of Structural Geology*, *78*, 52–66. https://doi.org/10.1016/j.jsg.2015.05.013

Bistacchi, A., Mittempergher, S., Martinelli, M., & Storti, F. (2020). On a new robust workflow for the statistical and spatial analysis of fracture data collected with scanlines (or the importance of stationarity). *Solid Earth*, *11*(6), 2535–2547. https://doi.org/10.5194/SE-11-2535-2020

Bonnet, E., Bour, O., Odling, N. E., Davy, P., Main, I., Cowie, P., & Berkowitz, B. (2001). Scaling of fracture systems in geological media. *Reviews of Geophysics*, *39*(3), 347–383.

https://doi.org/10.1029/1999RG000074

Bossennec, C., Frey, M., Seib, L., Bär, K., & Sass, I. (2021). Multiscale characterisation of fracture patterns of a crystalline reservoir analogue. *Geosciences (Switzerland)*, *11*(9), 1–23. https://doi.org/10.3390/geosciences11090371

Brace, W. F. (1984). Permeability of Crystalline Rocks: New in Situ Measurements. *Journal of Geophysical Research*, *89*(B6), 4327–4330. https://doi.org/10.1029/jb089ib06p04327

Cao, W., & Lei, Q. (2018). Influence of Landscape Coverage on Measuring Spatial and Length Properties of Rock Fracture Networks: Insights from Numerical Simulation. *Pure and Applied Geophysics*, *175*(6), 2167–2179. https://doi.org/10.1007/s00024-018-1774-4

Castaing, C., Halawani, M. A., Gervais, F., Chilès, J. P., Genter, A., Bourgine, B., et al. (1996). Scaling relationships in intraplate fracture systems related to Red Sea rifting. *Tectonophysics*, *261*(4), 291–314. https://doi.org/10.1016/0040-1951(95)00177-8

Ceccato, A., Viola, G., Antonellini, M., Tartaglia, G., & Ryan, E. J. (2021). Constraints upon fault zone properties by combined structural analysis of virtual outcrop models and discrete fracture network modelling. *Journal of Structural Geology*, *152*(September), 104444. https://doi.org/10.1016/j.jsg.2021.104444

Ceccato, A., Viola, G., Tartaglia, G., & Antonellini, M. (2021). In–situ quantification of mechanical and permeability properties on outcrop analogues of offshore fractured and weathered crystalline basement: Examples from the Rolvsnes granodiorite, Bømlo, Norway. *Marine and Petroleum Geology*, *124*(July 2020). https://doi.org/10.1016/j.marpetgeo.2020.104859

Chabani, A., Trullenque, G., Ledésert, B. A., & Klee, J. (2021). Multiscale characterization of fracture patterns: A case study of the noble hills range (Death valley, CA, Usa), application to geothermal reservoirs. *Geosciences (Switzerland)*, *11*(7), 25–27. https://doi.org/10.3390/geosciences11070280

Damsleth, E., Sangolt, V., & Aamodt, G. (1998). Sub-seismic faults can seriously affect fluid flow in the Njord field off Western Norway - A stochastic fault modeling case study. *Proceedings - SPE Annual Technical Conference and Exhibition*, *1999-Septe*, 295–304. https://doi.org/10.2523/49024-ms

Dershowitz, W. S., & Herda, H. H. (1992). Interpretation of fracture spacing and intensity. *The 33rd U.S. Symposium on Rock Mechanics (USRMS), Santa Fe, New Mexico, June 1992.*, 757–766. Retrieved from http://onepetro.org/ARMAUSRMS/proceedings-pdf/ARMA92/All-ARMA92/ARMA-92-0757/1987502/arma-92-0757.pdf

Dichiarante, A. M., McCaffrey, K. J. W., Holdsworth, R. E., Bjørnarå, T. I., & Dempsey, E. D. (2020). Fracture attribute scaling and connectivity in the Devonian Orcadian Basin with implications for geologically equivalent sub-surface fractured reservoirs. *Solid Earth*, *11*(6), 2221–2244. https://doi.org/10.5194/se-11-2221-2020

Fazlikhani, H., Fossen, H., Gawthorpe, R. L., Faleide, J. I., & Bell, R. E. (2017). Basement structure and its influence on the structural configuration of the northern North Sea rift. *Tectonics*, *36*(6), 1151–1177. https://doi.org/10.1002/2017TC004514

Fossen, H., Khani, H. F., Faleide, J. I., Ksienzyk, A. K., & Dunlap, W. J. (2016). Post-Caledonian extension in the West Norway-northern North Sea region: The role of structural inheritance. *Geological Society Special Publication*, *439*(1), 465–486. https://doi.org/10.1144/SP439.6

Fossen, H., Khani, H. F., Faleide, J. I., Ksienzyk, A. K., & Dunlap, W. J. (2017). Post-Caledonian extension in the West Norway-northern North Sea region: The role of structural inheritance. *Geological Society Special Publication*, *439*(1), 465–486. https://doi.org/10.1144/SP439.6

Fossen, H., Ksienzyk, A. K., Rotevatn, A., Bauck, M. S., & Wemmer, K. (2021). From widespread faulting to localised rifting: Evidence from K-Ar fault gouge dates from the Norwegian North Sea rift shoulder. *Basin Research*, *33*(3), 1934–1953. https://doi.org/10.1111/BRE.12541

854 Fredin, O., Viola, G., Zwingmann, H., Sørlie, R., Brönner, M., Lie, J. E., et al. (2017). The
855 inheritance of a mesozoic landscape in western Scandinavia. *Nature Communications*, *8*.
856 https://doi.org/10.1038/ncomms14879

857 Gabrielsen, R. H., & Braathen, A. (2014). Models of fracture lineaments - Joint swarms, fracture
858 corridors and faults in crystalline rocks, and their genetic relations. *Tectonophysics*, *628*, 26–
859 44. https://doi.org/10.1016/j.tecto.2014.04.022

860 Gabrielsen, R. H., Braathen, A., Dehis, J., & Roberts, D. (2002). Tectonic lineaments of Norway.
861 *Norsk Geologisk Tidsskrift*, *82*(3), 153–174.

862 Gabrielsen, R. H., Nystuen, J. P., & Olesen, O. (2018). Fault distribution in the Precambrian
863 basement of South Norway. *Journal of Structural Geology*, *108*, 269–289.
864 https://doi.org/10.1016/j.jsg.2017.06.006

865 Le Garzic, E., de L'Hamaide, T., Diraison, M., Géraud, Y., Sausse, J., de Urreiztieta, M., et al.
866 (2011). Scaling and geometric properties of extensional fracture systems in the proterozoic
867 basement of Yemen. Tectonic interpretation and fluid flow implications. *Journal of Structural*
868 *Geology*, *33*(4), 519–536. https://doi.org/10.1016/j.jsg.2011.01.012

869 Gee, D. G., Fossen, H., Henriksen, N., & Higgins, A. K. (2008). From the early Paleozoic platforms
870 of Baltica and Laurentia to the Caledonide Orogen of Scandinavia and Greenland. *Episodes*,
871 *31*(1), 44–51. https://doi.org/10.18814/epiiugs/2008/v31i1/007

872 Gillespie, P. A., Howard, C. B., Walsh, J. J., & Watterson, J. (1993). Measurement and
873 characterisation of spatial distributions of fractures. *Tectonophysics*, *226*(1–4), 113–141.
874 https://doi.org/10.1016/0040-1951(93)90114-Y

875 Hardebol, N. J., Maier, C., Nick, H., Geiger, S., Bertotti, G., & Boro, H. (2015). Multiscale fracture
876 network characterization and impact on flow: A case study on the Latemar carbonate platform.
877 *Journal of Geophysical Research: Solid Earth*, *120*(12), 8197–8222.

https://doi.org/10.1002/2015JB011879

Healy, D., Rizzo, R. E., Cornwell, D. G., Farrell, N. J. C., Watkins, H., Timms, N. E., et al. (2017). FracPaQ: A MATLAB™ toolbox for the quantification of fracture patterns. *Journal of Structural Geology*, *95*, 1–16. https://doi.org/10.1016/j.jsg.2016.12.003

Hirata, T. (1989). Fractal Dimension of Fault Systems in Japan: Fractal Structure in Rock Fracture Geometry at Various Scales. *Fractals in Geophysics*, 157–170. https://doi.org/10.1007/978-3-0348-6389-6_9

Holdsworth, R. E., McCaffrey, K. J. W., Dempsey, E., Roberts, N. M. W., Hardman, K., Morton, A., et al. (2019). Natural fracture propping and earthquake-induced oil migration in fractured basement reservoirs. *Geology*, *47*(8), 700–704. https://doi.org/10.1130/G46280.1

Holdsworth, R. E., Trice, R., Hardman, K., McCaffrey, K. J. W., Morton, A., Frei, D., et al. (2020). The nature and age of basement host rocks and fissure fills in the Lancaster field fractured reservoir, West of Shetland. *Journal of the Geological Society*, jgs2019-142. https://doi.org/10.1144/jgs2019-142

Kolyukhin, D., & Torabi, A. (2013). Power-Law Testing for Fault Attributes Distributions. *Pure and Applied Geophysics 2013 170:12*, *170*(12), 2173–2183. https://doi.org/10.1007/S00024-013-0644-3

Kruhl, J. H. (2013). Fractal-geometry techniques in the quantification of complex rock structures: A special view on scaling regimes, inhomogeneity and anisotropy. *Journal of Structural Geology*, *46*, 2–21. https://doi.org/10.1016/J.JSG.2012.10.002

Laubach, S. E., Olson, J. E., & Cross, M. R. (2009). Mechanical and fracture stratigraphy. *AAPG Bulletin*, *93*(11), 1413–1426. https://doi.org/10.1306/07270909094

Lundmark, A. M., Sæther, T., & Sørlie, R. (2014). Ordovician to silurian magmatism on the Utsira

High, North Sea: Implications for correlations between the onshore and offshore Caledonides. *Geological Society Special Publication*, *390*(1), 513–523. https://doi.org/10.1144/SP390.21

Manzocchi, T., Walsh, J. J., & Bailey, W. R. (2009). Population scaling biases in map samples of power-law fault systems. *Journal of Structural Geology*, *31*(12), 1612–1626. https://doi.org/10.1016/J.JSG.2009.06.004

Marrett, R., Gale, J. F. W., Gómez, L. A., & Laubach, S. E. (2018). Correlation analysis of fracture arrangement in space. *Journal of Structural Geology*, *108*, 16–33. https://doi.org/10.1016/J.JSG.2017.06.012

McCaffrey, K. J. W., Holdsworth, R. E., Pless, J., Franklin, B. S. G., & Hardman, K. (2020). Basement reservoir plumbing: fracture aperture, length and topology analysis of the Lewisian Complex, NW Scotland. *Journal of the Geological Society*. https://doi.org/https://doi.org/10.1144/jgs2019-143 This

Michas, G., Vallianatos, F., & Sammonds, P. (2015). Statistical mechanics and scaling of fault populations with increasing strain in the Corinth Rift. *Earth and Planetary Science Letters*, *431*, 150–163. https://doi.org/10.1016/J.EPSL.2015.09.014

Munro, M. A., & Blenkinsop, T. G. (2012). MARD-A moving average rose diagram application for the geosciences. *Computers and Geosciences*, *49*, 112–120. https://doi.org/10.1016/j.cageo.2012.07.012

Nyberg, B., Nixon, C. W., & Sanderson, D. J. (2018). NetworkGT: A GIS tool for geometric and topological analysis of two-dimensional fracture networks. *Geosphere*, *14*(4), 1618–1634. https://doi.org/10.1130/GES01595.1

Odling, N. E. (1997). Scaling and connectivity of joint systems in sandstones from western Norway. *Journal of Structural Geology*, *19*(10), 1257–1271. https://doi.org/10.1016/S0191-8141(97)00041-2

925 Odling, N. E., Gillespie, P., Bourgine, B., Castaing, C., Chilés, J. P., Christensen, N. P., et al.
926 (1999). Variations in fracture system geometry and their implications for fluid flow in
927 fractured hydrocarbon reservoirs. *Petroleum Geoscience*, *5*(4), 373–384.
928 https://doi.org/10.1144/petgeo.5.4.373

929 Osagiede, E. E., Rotevatn, A., Gawthorpe, R., Kristensen, T. B., Jackson, C. A. L., & Marsh, N.
930 (2020). Pre-existing intra-basement shear zones influence growth and geometry of non-
931 colinear normal faults, western Utsira High–Heimdal Terrace, North Sea. *Journal of Structural*
932 *Geology*, *130*, 103908. https://doi.org/10.1016/J.JSG.2019.103908

933 Pennacchioni, G., Ceccato, A., Fioretti, A. M., Mazzoli, C., Zorzi, F., & Ferretti, P. (2016).
934 Episyenites in meta-granitoids of the Tauern Window (Eastern Alps): unpredictable? *Journal*
935 *of Geodynamics*, *101*. https://doi.org/10.1016/j.jog.2016.04.001

936 Phillips, T. B., Jackson, C. A. L., Bell, R. E., Duffy, O. B., & Fossen, H. (2016). Reactivation of
937 intrabasement structures during rifting: A case study from offshore southern Norway. *Journal*
938 *of Structural Geology*, *91*, 54–73. https://doi.org/10.1016/J.JSG.2016.08.008

939 Place, J., Géraud, Y., Diraison, M., Herquel, G., Edel, J. B., Bano, M., et al. (2016). Structural
940 control of weathering processes within exhumed granitoids: Compartmentalisation of
941 geophysical properties by faults and fractures. *Journal of Structural Geology*, *84*, 102–119.
942 https://doi.org/10.1016/j.jsg.2015.11.011

943 Preiss, A. D., & Adam, J. (2021). Basement fault trends in the Southern North Sea Basin. *Journal of*
944 *Structural Geology*, *153*, 104449. https://doi.org/10.1016/J.JSG.2021.104449

945 Riber, L., Dypvik, H., & Sørlie, R. (2015). Altered basement rocks on the Utsira High and its
946 surroundings, Norwegian North Sea. *Norwegian Journal of Geology*, *95*(1), 57–89.
947 https://doi.org/10.17850/njg95-1-04

948 Rizzo, R. E., Healy, D., & De Siena, L. (2017). Benefits of maximum likelihood estimators for

fracture attribute analysis: Implications for permeability and up-scaling. *Journal of Structural Geology*, *95*, 17–31. https://doi.org/10.1016/j.jsg.2016.12.005

Sanderson, D. J., & Peacock, D. C. P. (2019). Line sampling of fracture swarms and corridors. *Journal of Structural Geology*, *122*(December 2018), 27–37. https://doi.org/10.1016/j.jsg.2019.02.006

Scheiber, T., & Viola, G. (2018). Complex Bedrock Fracture Patterns: A Multipronged Approach to Resolve Their Evolution in Space and Time. *Tectonics*, *37*(4), 1030–1062. https://doi.org/10.1002/2017TC004763

Scheiber, T., Fredin, O., Viola, G., Jarna, A., Gasser, D., & Łapińska-Viola, R. (2015). Manual extraction of bedrock lineaments from high-resolution LiDAR data: methodological bias and human perception. *Gff*, *137*(4), 362–372. https://doi.org/10.1080/11035897.2015.1085434

Scheiber, T., Viola, G., Wilkinson, C. M., Ganerød, M., Skår, Ø., & Gasser, D. (2016). Direct40Ar/39Ar dating of Late Ordovician and Silurian brittle faulting in the southwestern Norwegian Caledonides. *Terra Nova*, *28*(5), 374–382. https://doi.org/10.1111/ter.12230

Schneeberger, R., Egli, D., Lanyon, G. W., Mäder, U. K., Berger, A., Kober, F., & Herwegh, M. (2018). Structural-permeability favorability in crystalline rocks and implications for groundwater flow paths: a case study from the Aar Massif (central Switzerland). *Hydrogeology Journal*, *26*(8), 2725–2738. https://doi.org/10.1007/s10040-018-1826-y

Scholz, C. H. (2002). *The Mechanics of Earthquakes and Faulting (Second edition)*. *Cambridge University Press*. Retrieved from http://books.google.com/books?hl=en%7B&%7Damp;lr=%7B&%7Damp;id=JL1VM5wMbrQC%7B&%7Damp;oi=fnd%7B&%7Damp;pg=PR11%7B&%7Damp;dq=The+mechanics+of+earthquakes+and+faulting%7B&%7Damp;ots=tDcZRs3p2x%7B&%7Damp;sig=M-vxuJ99fg0ez086EuTvxsPvQJs

973 Schultz, R. A., Klimczak, C., Fossen, H., Olson, J. E., Exner, U., Reeves, D. M., & Soliva, R.
974 (2013). Statistical tests of scaling relationships for geologic structures. *Journal of Structural*
975 *Geology*, *48*, 85–94. https://doi.org/10.1016/J.JSG.2012.12.005

976 Slagstad, T., Davidsen, B., & Stephen Daly, J. (2011). Age and composition of crystalline basement
977 rocks on the norwegian continental margin: Offshore extension and continuity of the
978 Caledonian-Appalachian orogenic belt. *Journal of the Geological Society*, *168*(5), 1167–1185.
979 https://doi.org/10.1144/0016-76492010-136

980 Soliva, R., Benedicto, A., & Maerten, L. (2006). Spacing and linkage of confined normal faults:
981 Importance of mechanical thickness. *Journal of Geophysical Research: Solid Earth*, *111*(B1),
982 1402. https://doi.org/10.1029/2004JB003507

983 Souque, C., Knipe, R. J., Davies, R. K., Jones, P., Welch, M. J., & Lorenz, J. (2019). Fracture
984 corridors and fault reactivation: Example from the Chalk, Isle of Thanet, Kent, England.
985 *Journal of Structural Geology*, *122*(March 2015), 11–26.
986 https://doi.org/10.1016/j.jsg.2018.12.004

987 Stober, I., & Bucher, K. (2015). Hydraulic conductivity of fractured upper crust: Insights from
988 hydraulic tests in boreholes and fluid-rock interaction in crystalline basement rocks. *Geofluids*,
989 *15*(1–2), 161–178. https://doi.org/10.1111/gfl.12104

990 Tanner, D. C., Buness, H., Igel, J., Günther, T., Gabriel, G., Skiba, P., et al. (2019). *Fault detection*.
991 *Understanding Faults: Detecting, Dating, and Modeling*. https://doi.org/10.1016/B978-0-12-
992 815985-9.00003-5

993 Tartaglia, G., Viola, G., van der Lelij, R., Scheiber, T., Ceccato, A., & Schönenberger, J. (2020).
994 "Brittle structural facies" analysis: A diagnostic method to unravel and date multiple slip
995 events of long-lived faults. *Earth and Planetary Science Letters*, *545*, 116420.
996 https://doi.org/10.1016/j.epsl.2020.116420

997 Torabi, A., & Berg, S. S. (2011). Scaling of fault attributes: A review. *Marine and Petroleum*
998 *Geology*, *28*(8), 1444–1460. https://doi.org/10.1016/j.marpetgeo.2011.04.003

999 Trice, R., Hiorth, C., & Holdsworth, R. (2019). Fractured basement play development on the UK
1000 and Norwegian rifted margins. *Geological Society, London, Special Publications*, SP495-
1001 2018–174. https://doi.org/10.1144/sp495-2018-174

1002 Viola, G., Scheiber, T., Fredin, O., Zwingmann, H., Margreth, A., & Knies, J. (2016).
1003 Deconvoluting complex structural histories archived in brittle fault zones. *Nature*
1004 *Communications*, *7*, 1–10. https://doi.org/10.1038/ncomms13448

1005 Walsh, J. J., Watterson, J., Heath, A., Gillespie, P. A., & Childs, C. (1998). Assessment of the
1006 effects of sub-seismic faults on bulk permeabilities of reservoir sequences. *Geological Society*
1007 *Special Publication*, *127*, 99–114. https://doi.org/10.1144/GSL.SP.1998.127.01.08

1008 Xu, S.-S., Nieto-Samaniego, A. F., Alaniz-Álvarez, S. A., & Velasquillo-Martínez, L. G. (2006).
1009 Effect of sampling and linkage on fault length and length–displacement relationship.
1010 *International Journal of Earth Sciences 2005 95:5*, *95*(5), 841–853.
1011 https://doi.org/10.1007/S00531-005-0065-3

1012 Yielding, G., Needham, T., & Jones, H. (1996). Sampling of fault populations using sub-surface
1013 data: A review. *Journal of Structural Geology*, *18*(2–3), 135–146.
1014 https://doi.org/10.1016/S0191-8141(96)80039-3

1015